Upper mantle S velocity structure of North America

S. van der Lee[1] and G. Nolet

Department of Geosciences, Princeton University, Princeton, New Jersey

Abstract. We have inverted fundamental and higher-mode Rayleigh waveforms from 685 vertical component broadband seismograms with wave paths over North America to obtain an image of the upper mantle S velocity structure down to 660 km. Among the well-resolved features of the new model are (1) a high-velocity root beneath the North American craton which extends no deeper than 250 km except near the Archean core of the craton where depths of 350 km are reached, (2) a weak band of low-velocity along the eastern margin of the North American craton, which reaches into the transition zone, (3) a low velocity slab window beneath the western United States down to a depth of 300 km, (4) areas of low uppermost mantle velocity beneath the Cascade volcanoes, the Yellowstone hotspot track, the Colorado plateau, the Sierra Madre Occidental, and the grabens bordering the Jalisco block, and (5) a pronounced band of high velocities in the transition zone, coinciding with the expected location of the subducted trailing fragments of the Farallon plate. We introduce several improvements to the method of partitioned waveform inversion, which was used to compute the new model: rather than to correct for an estimated depth to the Mohorovičic discontinuity, we leave the crustal thickness as a free though yet poorly resolved parameter in the inversion; we also improve the windowing and filtering operator used to select uncontaminated waveforms.

1. Introduction

Early studies of the upper mantle beneath continents have revealed a strong age dependence of the shallow S velocity structure [Knopoff, 1972; Jordan, 1975]. Where older cratons are generally characterized by a thick, high-velocity lithosphere, Phanerozoic platforms have more normal velocities. Extensional provinces and rift zones are underlain by velocities so low that partial melting is often implied [e.g., Anderson and Spetzler, 1970; Priestley and Brune, 1978; Shankland et al., 1981; Hales, 1991; Humphreys and Dueker, 1994b; Saltzer and Humphreys, 1997]. The precise depth extent of the continental roots of cratons is still subject to debate [Jordan, 1988; Lerner-Lam and Jordan, 1987; VanDecar et al., 1995]. More recently, low velocities too have been shown to extend to large depth, i.e. the transition zone, at locations of recent or past subduction [Nolet and Zielhuis, 1994]. Much of the variability in upper mantle structure is still not well understood, and detailed images of upper mantle structure are needed to identify the dynamical and mineralogical processes that operate at depth.

The North American continent is an ideal region to obtain more detailed and reliable seismological information and increase our understanding of continental tectonics: it has a large density of modern, broadband, digital seismographs and areas of high seismicity abut on its south and west borders. In this paper we report on the three-dimensional (3-D) S velocity structure derived from the inversion of full wave trains of both fundamental and higher-mode Rayleigh waves from nearly 700 seismograms from ray paths on a continental scale. Although our results will eventually be combined with and refined by results from the interpretation of local seismograms [Das and Nolet, 1995], body waves, and scattered waves [Meier et al., 1997], they already reveal important information, for example, about the morphology of the North American craton, about the extent of the low velocities beneath the tectonically active western United States and northern Mexico, and about the subducted trailing fragments of the Farallon plate [Van der Lee and Nolet, 1997].

Our work on the 3-D upper mantle S velocity structure beneath North America fills the gap between global models, which do not have the resolution to reveal much more than low velocities in western North America and high velocities in eastern North America, and a large number of local studies, which reveal detailed structure in limited areas covered by dense instrumentation. It is well known that uppermost mantle velocities are extremely low in the western United States and northwestern Mexico compared to the eastern and central

[1]Now at Department of Terrestrial Magnetism, Carnegie Institution of Washington, Washington, D.C.

United States and Canada [*Cara*, 1979; *Walck* 1984; *Grand and Helmberger*, 1984; *Helmberger et al.*, 1985]. This has been confirmed by more recent continental-scale tomographic models [*Grand*, 1994; *Alsina et al.*, 1996].

Regional studies show variations in upper mantle structure at scale lengths less than a few hundreds of kilometers. For example, embedded in the low-velocity western United States upper mantle, *Humphreys and Dueker* [1994a] and *Benz et al.* [1992] have imaged regions of high P velocity. Farther north, the structure of the subducting Juan de Fuca slab has been imaged in detail [*Michaelson and Weaver*, 1986; *Rasmussen and Humphreys*, 1988; *Bostock and VanDecar*, 1995], while farther south the structure of the subducting Cocos slab has been mapped [*Van der Hilst*, 1990; *Pardo and Suárez*, 1995]. Our 3-D S velocity image of the North American upper mantle lacks the detail of the regional studies but is on a scale sufficiently large to connect these studies to regions of sparser seismic station coverage, such as southern, central, and eastern North America as well as to resolve structure in the transition zone.

2. Method

We apply the method of Partitioned Waveform Inversion (PWI), which has been introduced in detail by *Nolet* [1990]. In the first part of PWI the average velocity structure along each wave path is determined by optimally fitting the waveforms of each seismogram with synthetic waveforms. In the second part the path-averaged velocity structures for all paths are combined in a damped linear inversion for 3-D structure.

We construct synthetic seismograms by the summation of 20 mode branches, with phase velocities between 1 and 20 km/s. The mode branches have been discretized with frequency steps of 0.488 mHz for frequencies between 0.006 Hz and 0.08 Hz. This yields accurate seismograms, for a weakly heterogeneous Earth, in the limited time window from the S wave to the Rayleigh wave, for epicentral distances up to at least 70°. Our data contain paths of lengths between 4.5° and 94°, with a mean distance of 37° and only 15 paths with $\Delta > 71°$. Using a simulation of the effects of intermode scattering in two dimensions, *Kennett and Nolet* [1990] argue that waveform fitting of surface waves under the great circle approximation is safe for frequencies below 0.02 Hz for the fundamental mode and below 0.05 Hz for the higher modes, but they allow for somewhat more relaxed limits in a 3-D situation. Probably because we have shorter wave paths in our data set, the fundamental mode and/or higher modes in recorded seismograms often show coherence up to frequencies of 0.06 Hz. High-frequency (> 0.03 Hz) scattered waves often do not arrive until after the first part of the direct Rayleigh wave has arrived undisturbed. The improvements in windowing and filtering discussed in the appendix make it possible to cut the seismogram at any point within the Rayleigh wave, only considering the direct undisturbed part in the waveform fitting process.

Consequently we have fitted seismograms in frequency bands with lower limits ranging between 0.006 and 0.01 Hz and higher limits between 0.03 and 0.06 Hz. Some 10% of the paths are sufficiently short that we have allowed upper frequency limits up to 0.08 Hz. For the construction of synthetic seismograms we used a range of very similar background models with different crustal thicknesses. One of these, MC35, is also used as background model in the 3-D inversion and is shown for reference in Figure 1a and 1b. The other models in Figure 1 are discussed later. MC35 is based on the continental Earth model PEM-C [*Dziewonski et al.*, 1975] but has a constant uppermost mantle S velocity of 4.5 km/s down to 210 km replacing the high- and low-velocity zone of PEM-C. Using different background models for each ray path improves the initial fits substantially and reduces effects possibly introduced by nonlinearities. In addition, we account for local Earth structure beneath the source and station by assuming local Earth models to compute excitation factors and station amplitudes [*Levshin*, 1985; *Tromp and Dahlen*, 1992]. *Kennett* [1995] argues that such a local approximation is warranted for frequencies below 0.03 Hz.

We incorporate several improvements with respect to the earlier paper by *Zielhuis and Nolet* [1994]. In addition to improving the filtering and windowing operator needed to screen unmodeled wave energy, we parametrized the 3-D Earth in a Cartesian framework rather than with cells of variable width. The spacing between the knots of this Cartesian grid is 100 km in the x and y directions and 60 km in the z direction. In the damped linear inversion, we searched for an a priori smooth model. We also apply column scaling to precondition the linear equations. To avoid biasing our model with an interpreted crustal model, we allowed the crustal velocity and the Mohorovičic discontinuity (Moho) depth to vary in the inversion. Although our present data set does not sufficiently reduce the trade-offs between crustal velocity, Moho depth, and uppermost mantle velocity, this approach enables a future merge of our constraints with those from additional data that are targeted to constrain shallow structure. In this paper, we shall not discuss the structure directly below the crust, which might still be affected by a crustal signal. For as far as we deviate from *Nolet* [1990], further details of the inversion are described in the appendix.

3. Data Selection and Inversion

We use intermediate-period, vertical component seismograms for which most of the great circle ray path lies within the North American tectonic plate. The time window selected includes the fundamental Rayleigh mode as well as enough higher Rayleigh modes to model the multiple S waves and sometimes also the direct S wave. We have fitted the waveforms of 685 seismograms from 76 events and 70 stations. Only events with a surface wave or body wave magnitude over 5.5 have been considered (with three exceptions at favorable locations),
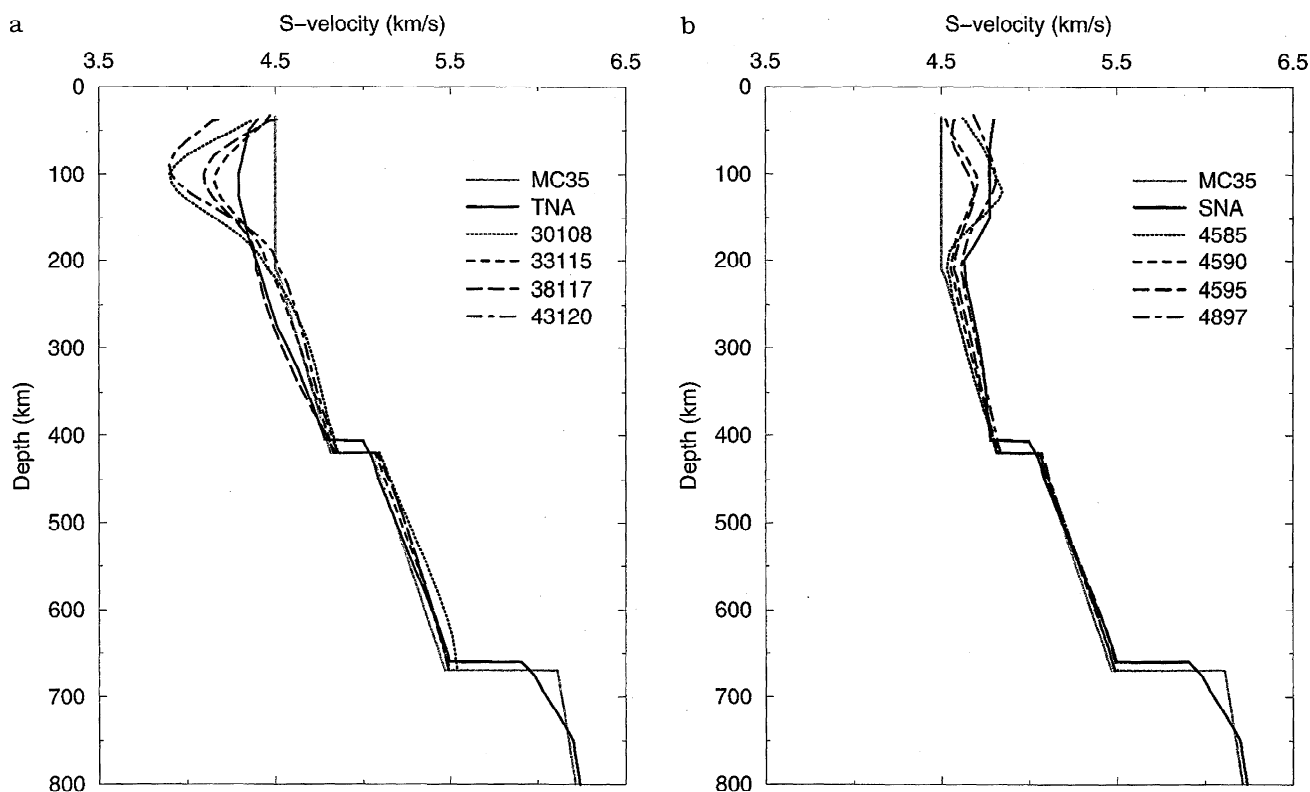
Figure 1. (a) Reference S velocity model MC35 and vertical profiles through NA95 at (45°N, 85°W), (45°N, 90°W), (45°N, 95°W), and (48°N, 97°W) compared to SNA. (b) Reference S velocity model MC35 vertical profiles through NA95 at (30°N, 108°W), (33°N, 115°W), (38°N, 117°W), and (43°N, 120°W) compared to TNA.

and the magnitude range has been limited to $M_s < 7$ (with one exception) to avoid any complications posed by a finite source size. The events are listed in Table 1 and the great circle ray path coverage is shown in Figure 2.

The data sources are the National Earthquake Information Center (NEIC), the Global Seismographic Network of the Incorporated Research Institutions for Seismology (IRIS/GSN), the U.S. National Seismograph Network (USNSN) and the Canadian National Seismic Network (CNSN). The U.S. Geological Survey/NEIC compact disks span a time period from 1980 to 1987. Most of these data are recorded by the Global Digital Seismograph Network (GDSN) and the Regional Seismic Test Network (RSTN) [Ahern at al., 1994]. Improved instrument responses for these recordings were obtained from R. Woodward (personal communcation, 1994) and Woodward and Masters [1989]. For the time period 1992-1995 we retrieved GSN data and corresponding instrument responses from the IRIS Data Management Center. We obtained additional data from the USNSN. A problem with the timekeeping of the long period USNSN instruments was discovered when we noted a mismatch between results from USNSN and other sources. The data loggers have since been fixed and the data used in this study have been corrected (R. Buland, personal communication, 1995). A few seismograms from the CNSN were obtained from M. Bo-

stock (personal communication, 1995). Standard CNSN instrument responses with unknown gain have been used, resulting in relative waveform fits for the CNSN data, while for data from the other sources the gain-corrected ground displacement amplitudes have been fit. Through primary data inspection we rejected the seismograms with clipped and nonseismic signals.

For the source orientation, we generally used the Harvard Centroid Moment Tensor solutions [Dziewonski et al., 1983] including the assumed half duration. We used the event locations as listed in Table 1, some of which are centroid locations and some are locations determined by the NEIC. Errors introduced by location errors average out in the 3-D inversion if they have a random character. A large variance often exists for reported event depths in the International Seismological Centre bulletins, and when necessary, we adapted the published depths, within their range of uncertainty, to the one that gave the best initial match to the observed waveform. Likewise, we checked the falloff of the amplitude spectra and adjusted the assumed half duration time, when needed, to match the data better.

3.1. Linear Constraints Along the Path

After data processing and fitting, we obtained 7535 constraints on 3-D North American upper mantle structure. A linear inversion of these constraints (see the appendix) resulted in NA95, our 3-D S velocity model for

Table 1. List of Events

Event ID[a]	Origin time, UT	Latitude	Longitude	Depth, km	m_b	M_s
800101	16 42:40.0	38.82	-27.78	10.0	6.0	6.7
800326	20 43:36.4	23.86	-45.57	10.0	5.9	6.3
800809	05 45:07.8	15.93	-88.52	9.3	6.1	6.4
810102	07 37:00.4	2.13	-79.16	5.0	5.7	5.7
810306	19 42:59.5	3.89	-85.92	11.0	6.1	6.4
810426	12 09:28.4	33.13	-115.65	6.0	5.5	6.0
810817	02 18:58.8	14.52	-93.77	10.0	5.6	5.6
810913	09 19:30.9	24.87	-46.30	6.0	5.8	5.5
810930	11 53:26.9	37.59	-118.89	5.0	5.6	5.8
811103	13 47:34.1	43.54	-127.71	10.0	5.9	6.2
820112	05 48:17.6	13.16	-87.59	8.0	5.8	6.0
820129	22 32:06.0	25.51	-45.29	5.0	5.7	5.8
820410	16 25:33.6	17.38	-83.50	10.0	5.8	5.9
820819	15 59:01.5	6.72	-82.68	14.0	6.3	6.5
830124	08 17:39.6	16.15	-95.23	36.0	6.3	6.6
830411	08 18:10.1	10.42	-62.76	40.0	6.0	5.8
830502	23 42:37.9	36.24	-120.30	12.0	6.2	6.5
830509	15 53:03.7	8.26	-82.95	35.0	5.5	6.1
830509	20 09:15.4	19.98	-109.45	10.0	5.5	6.2
830512	10 51:50.0	17.61	-46.55	7.0	5.6	5.7
830703	17 14:23.2	9.65	-83.69	33.0	5.7	6.1
830722	02 39:53.7	36.23	-120.41	9.2	6.0	5.7
830824	13 36:30.9	40.31	-124.77	30.0	5.5	5.7
831011	22 41:11.0	27.16	-44.50	8.0	5.5	5.6
831028	14 06:06.6	44.06	-113.86	10.0	6.2	7.3
831122	14 20:58.8	0.42	-79.94	23.3	6.3	6.2
831126	20 18:23.5	7.39	-82.26	10.0	5.6	6.0
831220	10 41:09.5	40.41	-124.90	5.0	5.6	5.5
840210	16 51:21.2	28.33	-112.08	10.0	5.6	6.2
840217	20 33:41.6	20.50	-109.23	10.0	5.5	5.5
840424	21 15:19.0	37.32	-121.70	8.0	5.8	6.1
840624	11 17:11.9	18.02	-69.30	25.0	6.0	6.7
840702	04 50:42.6	16.76	-98.51	34.6	5.8	6.0
840830	12 28:39.7	54.11	-133.64	10.0	5.5	5.6
840910	03 14:09.0	40.35	-126.86	10.0	6.2	6.7
841013	17 18:14.2	15.06	-94.24	30.9	6.1	5.7
841123	18 08:24.8	37.40	-118.51	5.0	5.6	5.7
841202	06 09:44.1	20.42	-115.75	10.0	6.0	6.3
850105	11 11:31.1	10.17	-80.02	32.3	6.2	5.7
850110	17 47:56.1	10.83	-43.43	10.0	5.8	5.8
850313	19 34:57.8	43.51	-127.50	10.0	6.1	6.3
850316	14 54:01.1	17.07	-62.41	14.1	6.2	6.3
850420	18 23:48.6	8.98	-77.53	40.4	5.6	5.9
850922	18 23:12.2	12.49	-44.33	10.0	5.7	5.5
851005	15 24:02.2	62.26	-124.31	6.0	6.5	6.6
851216	02 44:35.7	11.72	-85.85	20.5	5.9	6.0
851223	05 16:03.9	62.21	-124.30	6.0	6.4	6.9
860430	07 07:18.8	18.41	-102.98	32.3	6.2	7.0
860505	05 46:37.2	18.24	-102.53	10.0	5.6	5.6
870104	17 52:36.6	5.92	-82.67	10.0	5.5	5.9
870306	01 54:50.8	0.13	-77.67	13.8	6.1	6.1
870312	12 18:11.9	15.72	-94.50	33.0	5.7	5.6
870315	05 11:17.3	15.67	-94.52	38.0	5.6	5.6
920102	16 40:40.6	48.74	-129.23	10.0	5.7	6.0
920102	19 41:45.0	5.64	-73.83	134.0	5.8	
920115	06 58:32.4	18.02	-70.62	15.0	5.8	5.2
930515	21 52:25.3	51.37	-178.67	32.0	6.2	6.5
930903	12 35: 0.2	14.52	-92.71	27.0	5.8	6.8
931012	19 51:25.3	4.20	-76.64	103.0	5.4	
940302	03 38:03.8	19.80	-72.80	59.0	5.3	
940314	20 51:24.9	15.99	-92.43	164.0	5.9	6.2
940606	20 47:40.5	2.92	-76.06	12.0	6.4	6.4
940901	15 15:53.0	40.40	-125.68	10.0	6.6	7.0
941027	17 45:58.0	43.52	-127.43	20.0	5.6	6.0

Table 1. (continued)

Event ID[a]	Origin time, UT	Latitude	Longitude	Depth, km	m_b	M_s
941210	16 17:41.0	18.24	-101.35	67.0	6.5	
950116	18 14:49.4	51.24	179.17	33.0	5.6	6.1
950119	15 05:03.6	5.08	-72.92	18.0	6.3	6.6
950208	18 40:24.6	4.19	-76.63	64.0	6.3	
950219	04 03:15.9	40.56	-125.56	10.0	6.0	6.8
950314	17 33:50.1	54.83	-161.27	33.0	6.1	5.9
950414	00 32:53.8	30.20	-103.32	5.0	5.6	5.7
950417	07 14:35.3	33.80	-38.60	10.0	5.8	5.7
950524	11 02:12.9	61.00	-150.12	42.0	5.3	5.0
950630	11 58:56.0	24.57	-110.29	10.0	5.9	6.2
950819	21 43:32.6	5.11	-75.67	125.0	6.2	
950828	10 46:10.6	25.97	-110.31	10.0	5.7	6.2

[a]Event ID contains year, month, and day; read 800101 as January 1, 1980.

North America. Some of the better waveform fits are shown in Figure 3 for the August 19, 1995, Colombia event and in Figure 4 for the June 30, 1995, event in the Gulf of California. The fit of the synthetic waveforms to the data is very good for both the Rayleigh wave and the higher modes. Simultaneously fitting the fundamental and higher modes provides good radial (depth) resolution because the fundamental mode is very sensitive to uppermost mantle structure while the higher modes are also sensitive to deeper structure. In the waveforms from the Colombia event to western United States stations (Figure 3, SMTC through COR, except FFC) one can see that the first arriving wave in the windows shown (the SS wave) arrives a few seconds earlier than predicted by the initial synthetics while the fundamental mode Rayleigh wave, at the end of the win-

dows shown, and the higher S multiples in between the SS wave and the fundamental mode, arrive much later than predicted by the initial synthetics. This is consistent with NA95, which shows, between Colombia and the western United States, very low velocities in the top 300 km and high velocities in the deeper upper mantle.

With few exceptions we did not include body waves with a turning point far below the 660 km discontinuity, to avoid artifacts introduced by ignoring the 2-D nature of the sensitivity kernel [*Marquering and Snieder*, 1994], and we make no attempt to image the lower mantle.

3.2. Resolution

To assess the data resolution, we used tests in which a known Earth model is used to compute synthetic data q'. To these, we have added normally distributed noise,
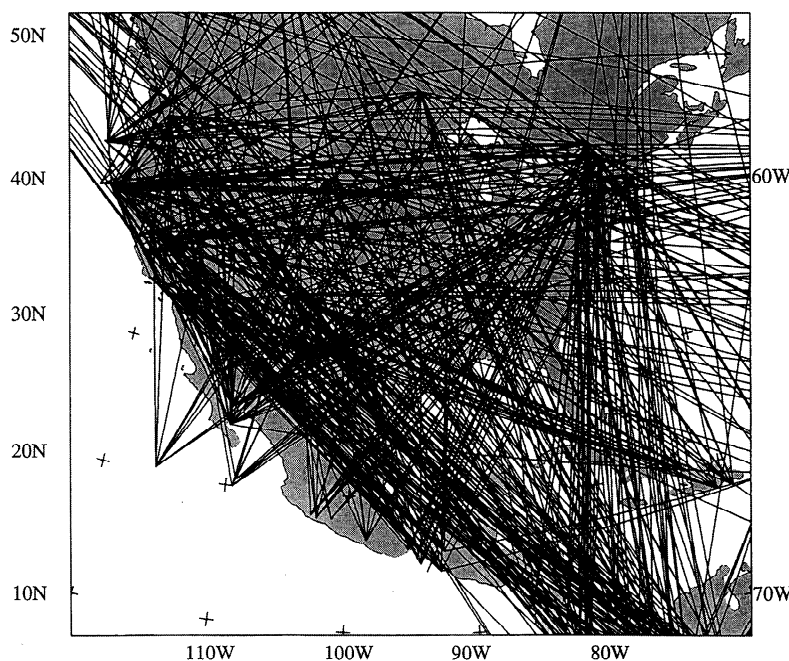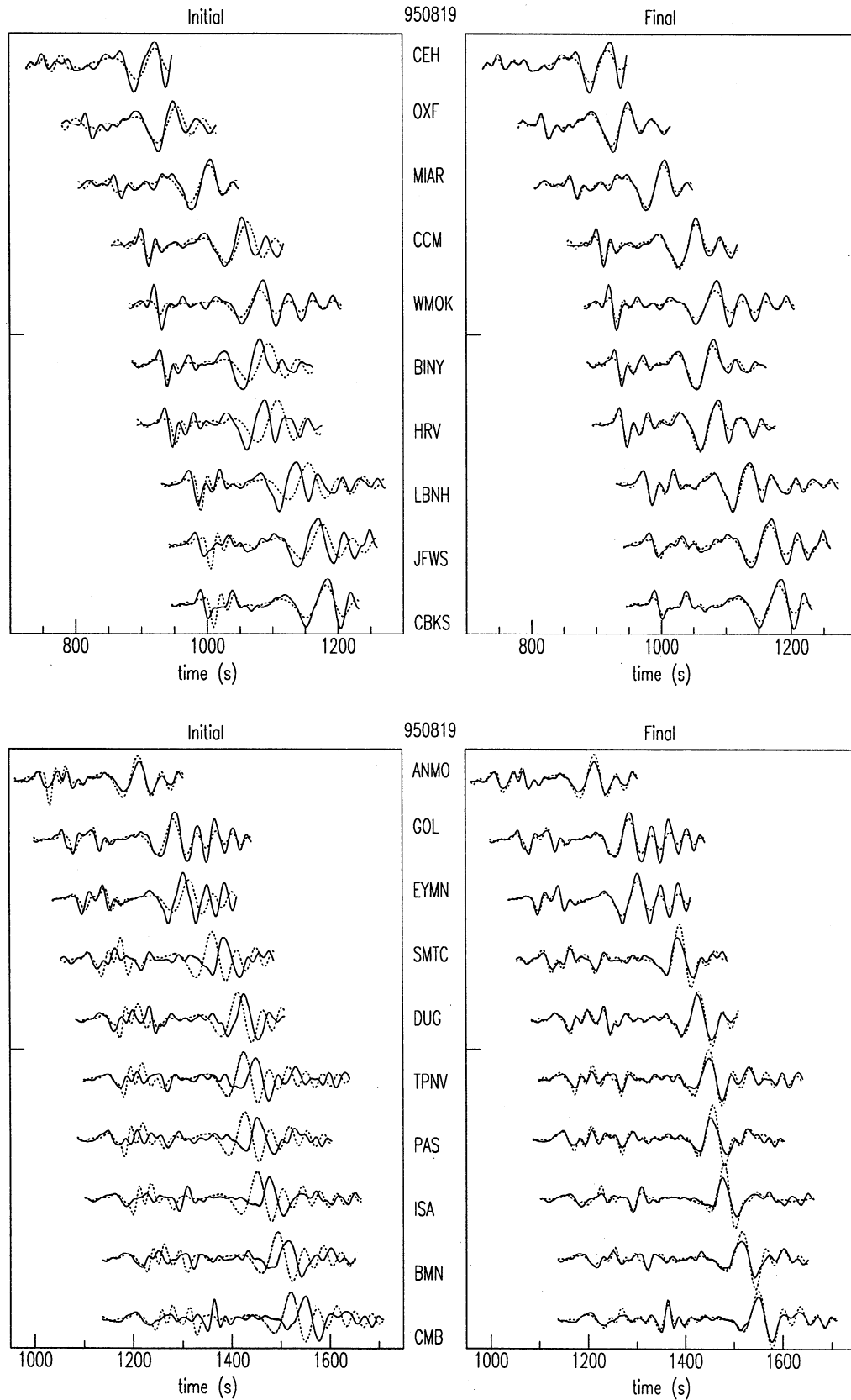

Figure 2. The great circle ray paths for the 685 seismogram used in this study.

Figure 3. (left) Initial waveforms and (right) waveforms fits for the August 19, 1995, Colombia event. The solid and dashed lines represent the data and synthetic waveforms, respectively. Stations have been ordered according to epicentral distance. Stations CEH is at 31°, with a predicted arrival for the S wave at 661 s, station BORG is at 71° where the S wave is expected to arrive at 1209 s. Unlike the example shown here, we have generally not included the S wave in our inversions when it has a turning point in the lower mantle.
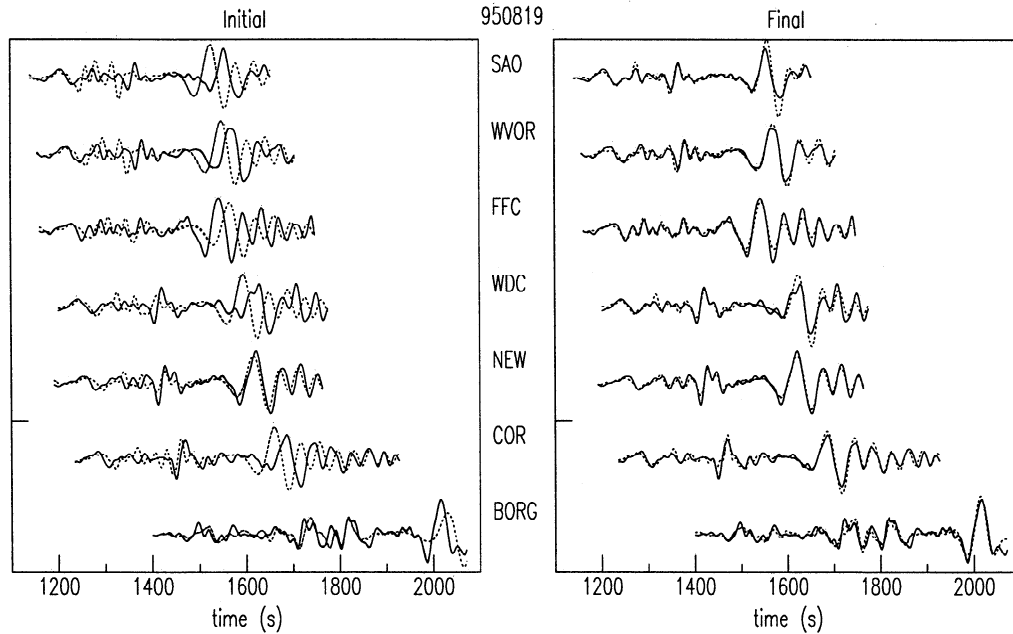
Figure 3. (continued)

with a standard deviation scaled by $|q'|/|q|$, and the inversion is performed completey analogous to that of the real data (see the appendix). The result of the inversion of the linear system (A37) depends on the value for the damping parameter λ. Figure 5 shows the variance reduction and model norm with proceeding iterations. We have conservatively chosen $\lambda = 1.4$, rather than the standard $\lambda = 1.0$, because it still provides a large variance reduction of 84%. An inversion with no damping and no column scaling was halted when it iterated to 84% variance reduction and gave very similar results,

also at transition zone depths, which indicates that our model is robust.

The models retrieved from the synthetic inversions indicate how well we can resolve particular structures. Figure 6 and 7 and Plate 1 show the results for a spike resolution test, a harmonic resolution test and a test of the resolution of structure similar to that sensed by our waveform data. The amplitudes of the anomalies in the retrieved models are consistently underestimated by various amounts. Here we are mainly concerned with the spatial resolution. Figure 2 shows that the United
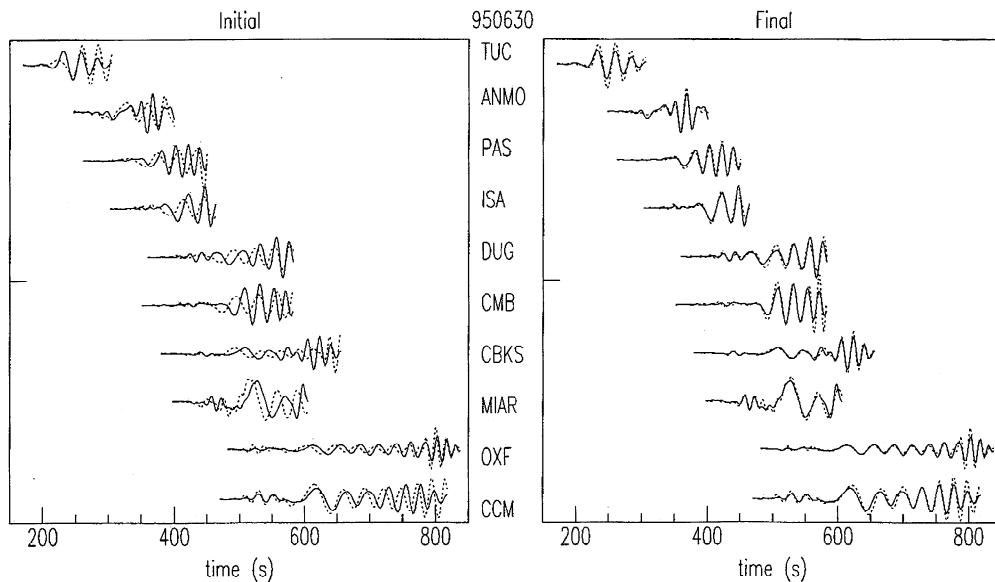
Figure 4. As Figure 3 for the June 30, 1995, event in the Gulf of California. The extreme stations TUC and COL are at 8° and 47°, while the S wave is expected to arrive at 201 s and 923 s, respectively.
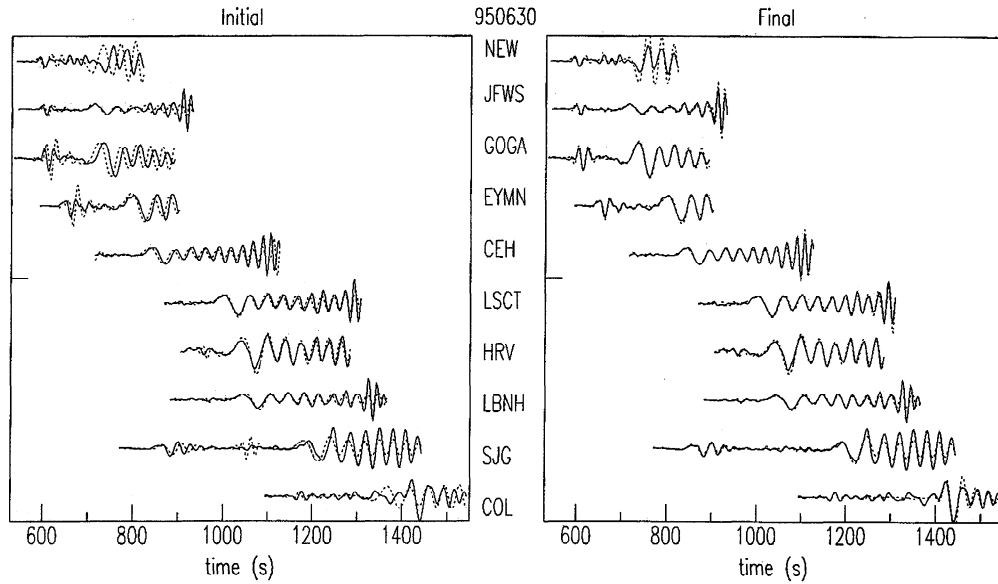
Figure 4. (continued)

States, northern Mexico, and the Gulf of Mexico are very well covered by rays. We expect the best resolution for this area. This is confirmed by a resolution test in which the synthetic input model has a constant S velocity anomaly for all knots of the grid. The retrieved structure is rather homogeneous, although underestimated in amplitude at transition zone depths. Thus no major structural biases are introduced by the ray geometry and sensitivity of the data. Although the synthetic

input models have no perturbations in crustal thickness, the resolved models have perturbations of no more than a couple of km.

It is clear from Figures 6 and 7 and Plate 1 that the resolution decreases with increasing depth. This is due to the fact that the bulk sensitivity of the data to structure, as measured by the c_j (A35), decreases with increasing depth [*Van der Lee*, 1996]. However, owing to the inclusion of constraints from higher-mode
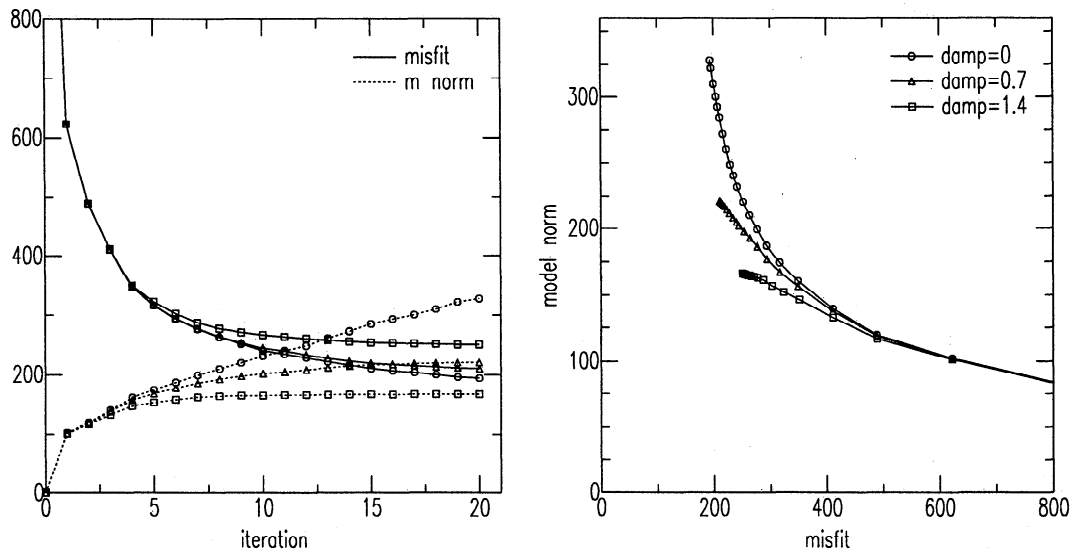
Figure 5. Dependence of the convergence of the linear inversion (A37) on the damping parameter λ. (left) Misfit and model norm plotted as a function of the iteration. (right) The model norm plotted as a function of the misfit; iterations proceed from right to left. In both graphs the initial misfit of 1618 (corresponding to a model norm of 0) is beyond the scale of the frame. The units for model norm and misfit are arbitrary. For $\lambda = 0$, no convergence is reached within 20 iterations, whereas the norm of the model grows fast. For $\lambda = 0.7$ the model norm is suppressed, while the misfit continues to creep to lower values as iterations proceed. For $\lambda = 1.4$, convergence is reached after about 15 iterations. After the 15th iteration, less than 0.1 % variance reduction is achieved in the next 35 iterations.
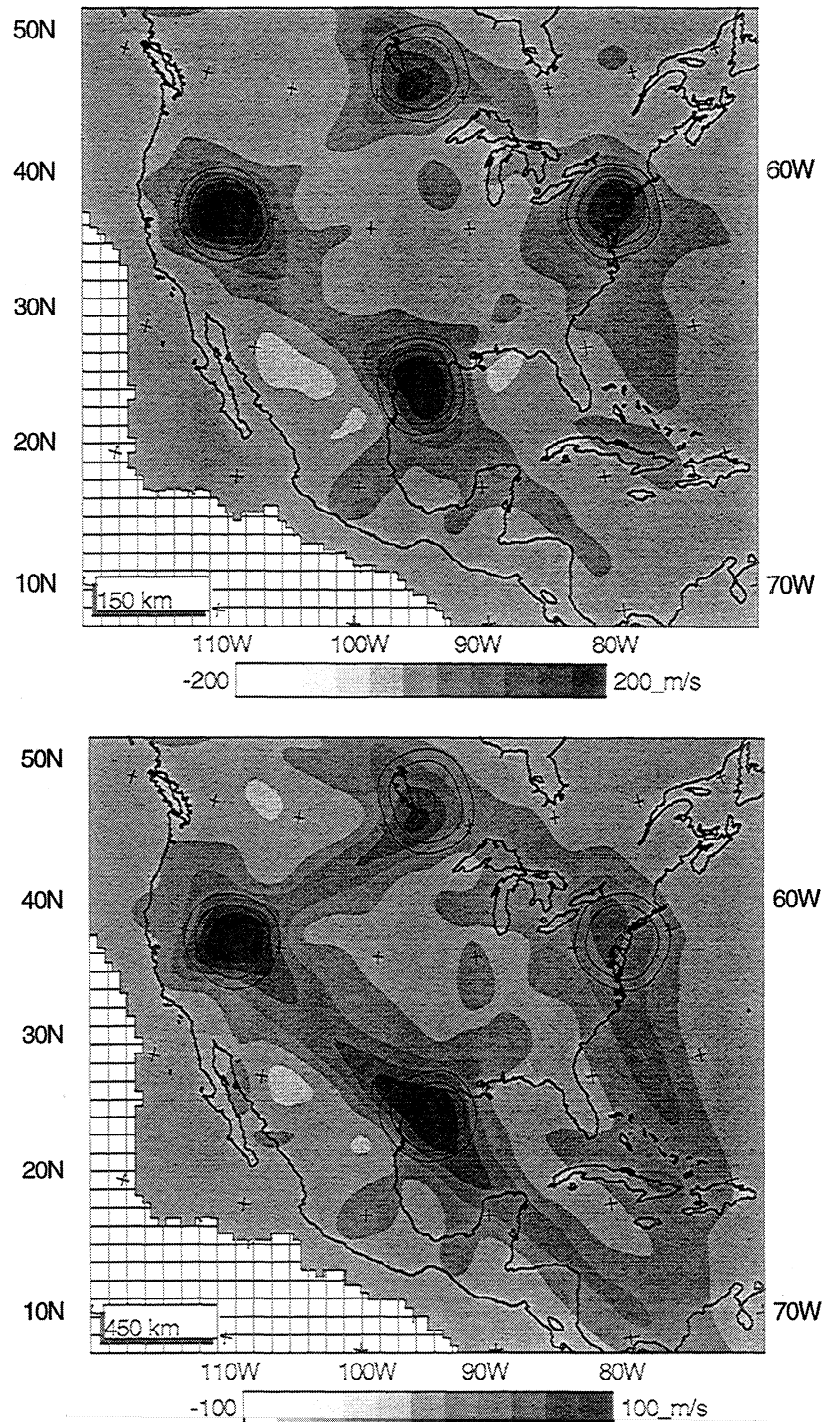
Figure 6. Results from the spike resolution test at depths of 150 and 450 km are labeled. The spikes in the input model are contoured at 100, 200, and 300 m/s. The output model is plotted in grey shades according to the legend.

waveforms, the sensitivity at depth is still significant and useful resolution exists for the deeper upper mantle, as shown by Figures 6 and 7 and Plate 1. The inversions for the tests shown in these figures and plate converge within about 10 iterations to variance reductions of 87%, 80% and 91%, respectively.

In the spike resolution test (Figure 6) the input spikes have a diameter of roughly 500 km and are very well re-

solved in the western United States, both in the uppermost mantle and in the transition zone. The resolution for other areas is also good, although some smearing occurs along the dominant directions of the rays, notably in the transition zone south of 15°.

The resolution also decreases in the Atlantic. Structure we find for the Atlantic should thus be considered merely as averaged over the dominant east-west direc-
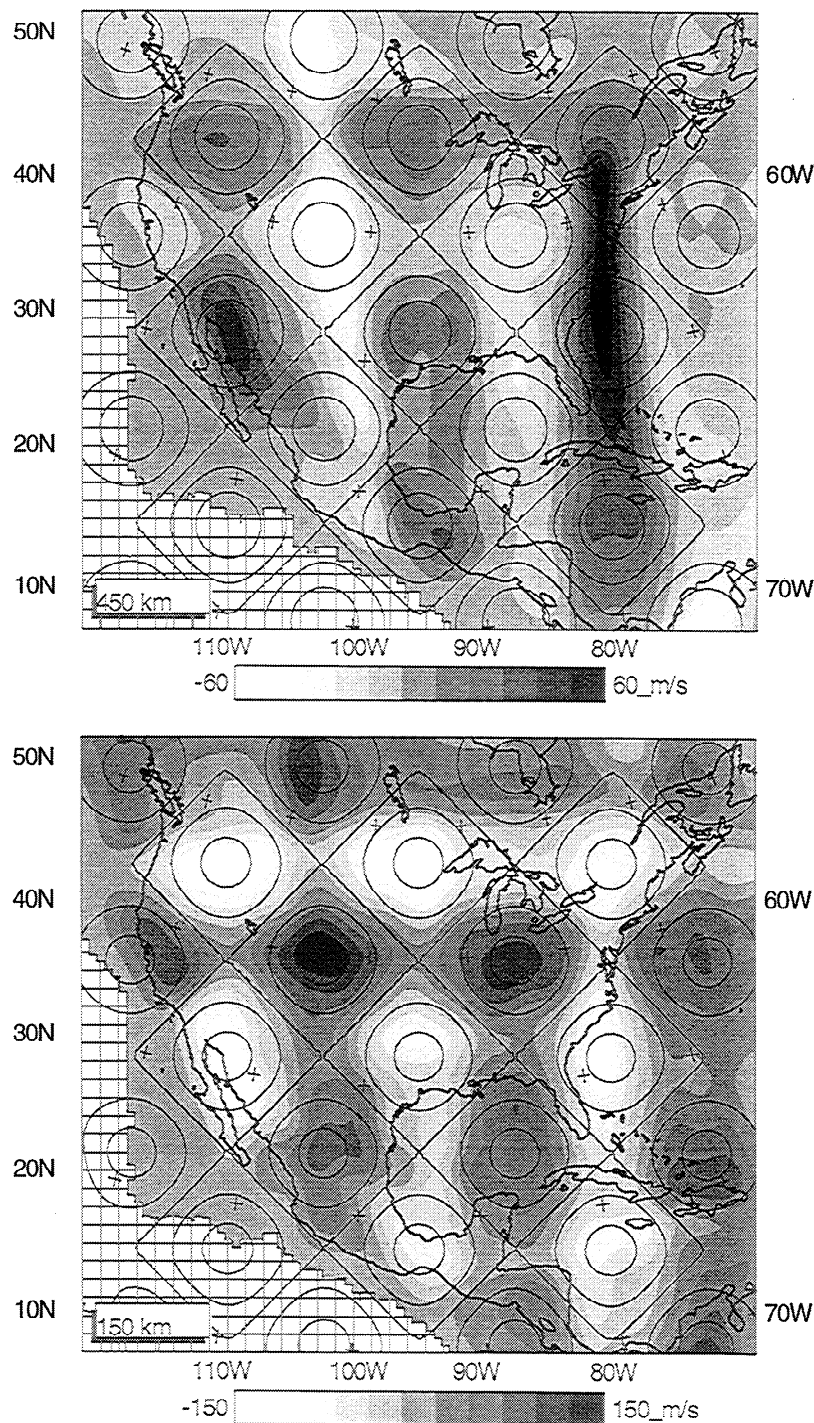
Figure 7. As Figure 6, for the harmonic resolution test. The input model is contoured at -200, -100, 0, 100, and 200 m/s.

tion of the ray paths, and lateral variations on scales of a few hundreds of kilometers cannot be considered resolved.

The harmonic pattern (Figure 7) has a wavelength of 2000 km and the results from the resolution test are comparable to those of the spike test. The resolution for the uppermost mantle is very good for the entire United States, good for Mexico, and reasonable for southwestern Canada. This indicates that for the uppermost mantle we have resolving power up to at least spherical harmonic degree 20. In the transition zone the unre-

alistic harmonic structure is harder to resolve due to lower sensitivity of the waveforms at these depths [*Van der Lee*, 1996]. The resolution in the transition zone is still good for the western United States, but in Mexico southward smearing begins to play a role. There is no resolution, at transition zone depths, for Jalisco and surrounding area nor for the Gulf of Mexico, Caribbean, and Atlantic at transition zone depths.

We further investigated the resolution using synthetic models with more realistic anomalies, i.e., an area of low uppermost mantle velocities beneath the western
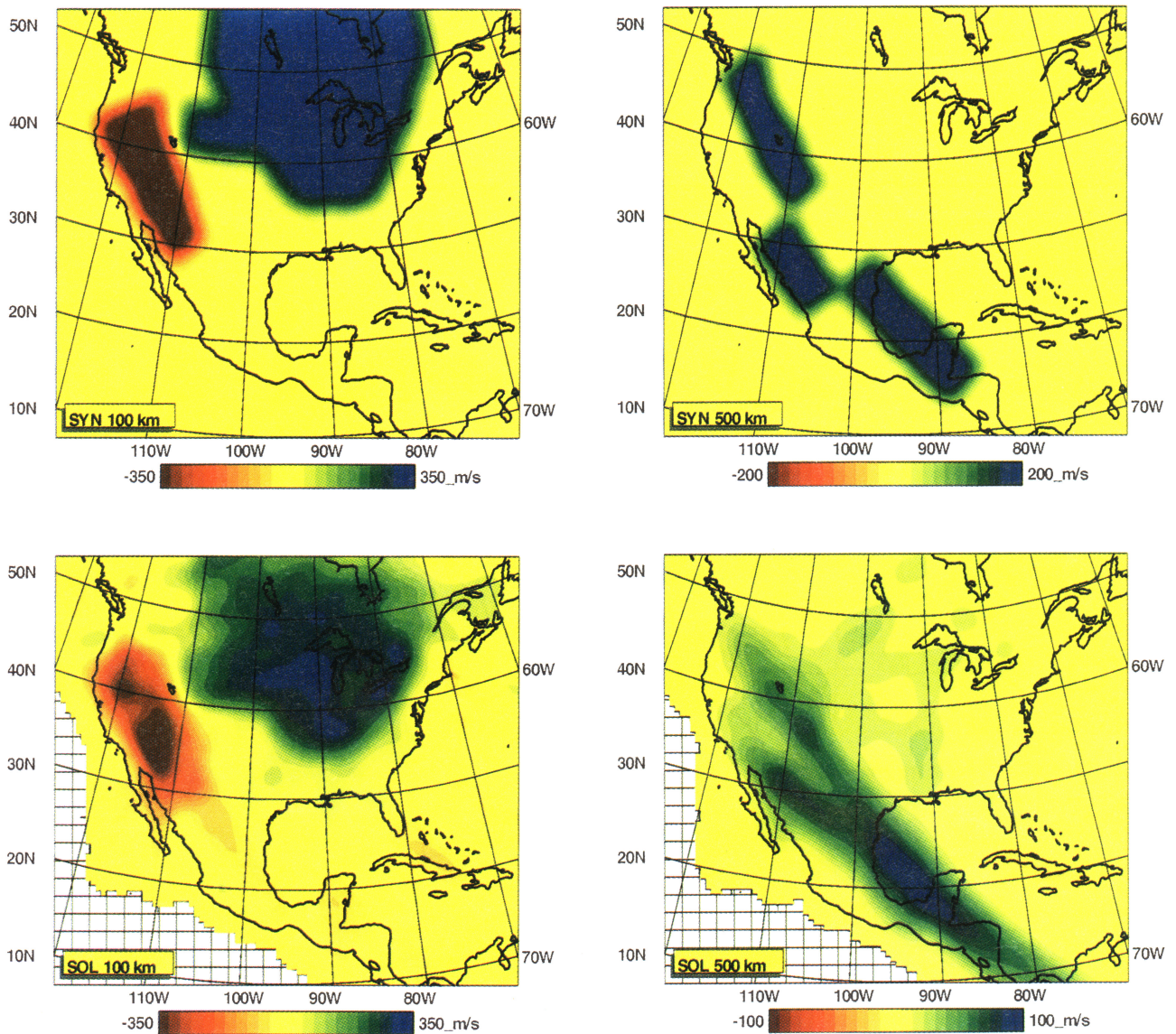
Plate 1. Results from a synthethic test designed to assess the reliability of structure visible in model NA95. SYN labels the input model and SOL labels the retrieved model. (left) A cratonic root and a low-velocity region under the western United States, at a depth of 100 km. (right) A structure possibly representative of the 500 km deep tail end of the subducted Farallon plate. These structures are also shown in vertical cross sections in Plates 3–5.

United States, an area of high upper-mantle velocities with a depth dependence as in model SNA, derived by *Grand and Helmberger* [1984] (Figure 1a) for the tectonically stable part of North America, and a banded structure of high velocities at transition zone depths. Plate 1 shows that the resolution for the uppermost mantle is excellent. However, sharp edges, such as for the extension of the high-velocity anomaly beneath Wyoming, are smoothed out while the resolution generally decreases north of 52°N. We shall address the resolution of more specific features of our final model in the next section.

3.3. A Posteriori Waveform Fits

With a variance reduction of 84%, our final solution falls short of a perfect solution to the undamped system

(A20). Therefore the original waveform fits no longer hold, and recomputed, a posteriori waveform fits are shown for the events discussed earlier in Figures 8 and 9. In general, the a posteriori fits are still acceptable. Figures 8 and 9 show that the a posteriori fits for the data from Figures 3 and 4 are very good. We analyzed the locations of ray paths with the worst a posteriori fits, but these do not show a clear correlation with geography, in contrast to the finding by *Zielhuis and Nolet* [1994], who show that the largest misfits in Europe are concentrated around the Mediterranean. This may partly be due to the improvements in windowing the data which reduces the impact of scattered wave energy; it may also indicate that the upper mantle under North America lacks regions of complexity as extreme as found in the Mediterranean.
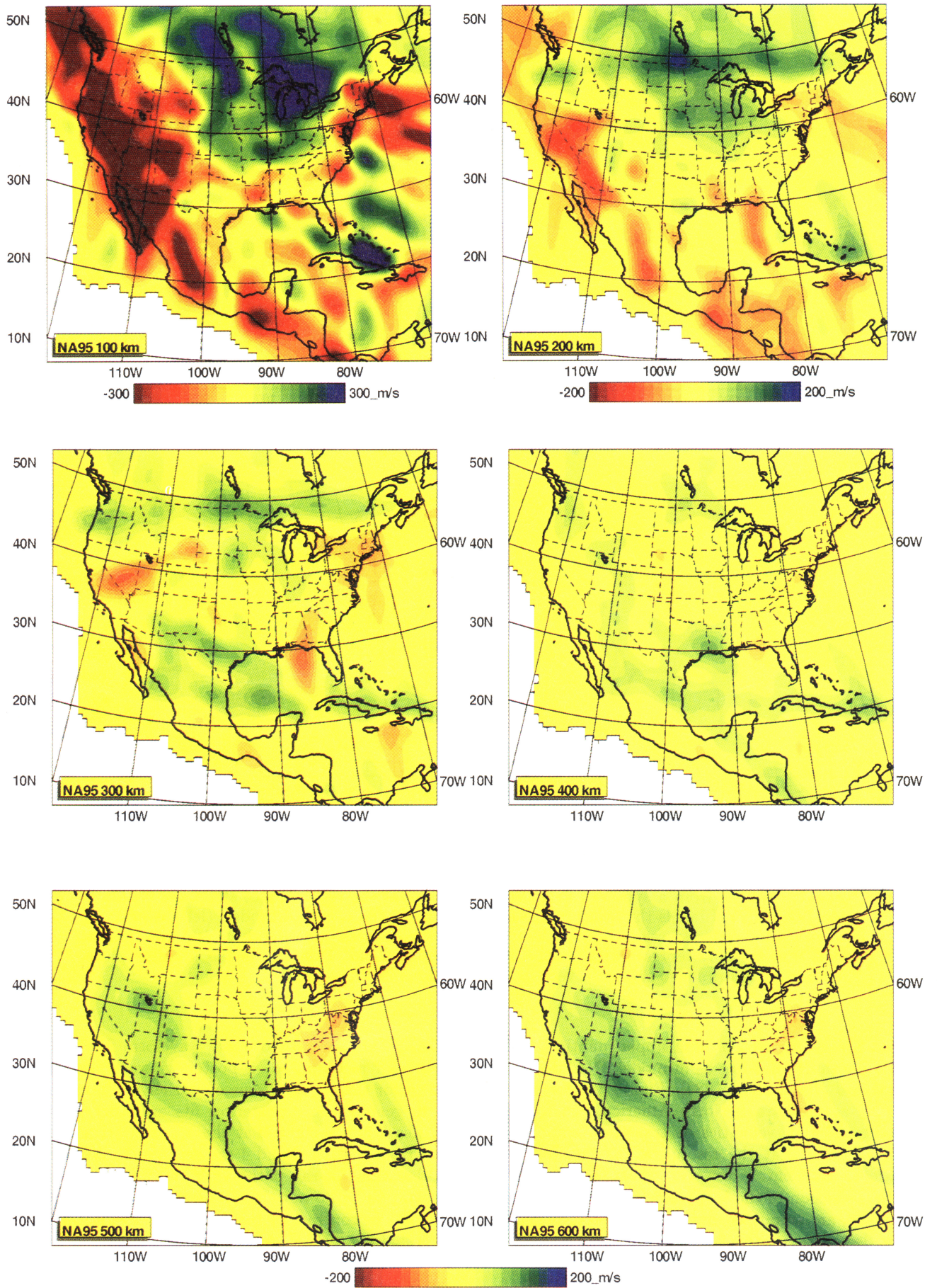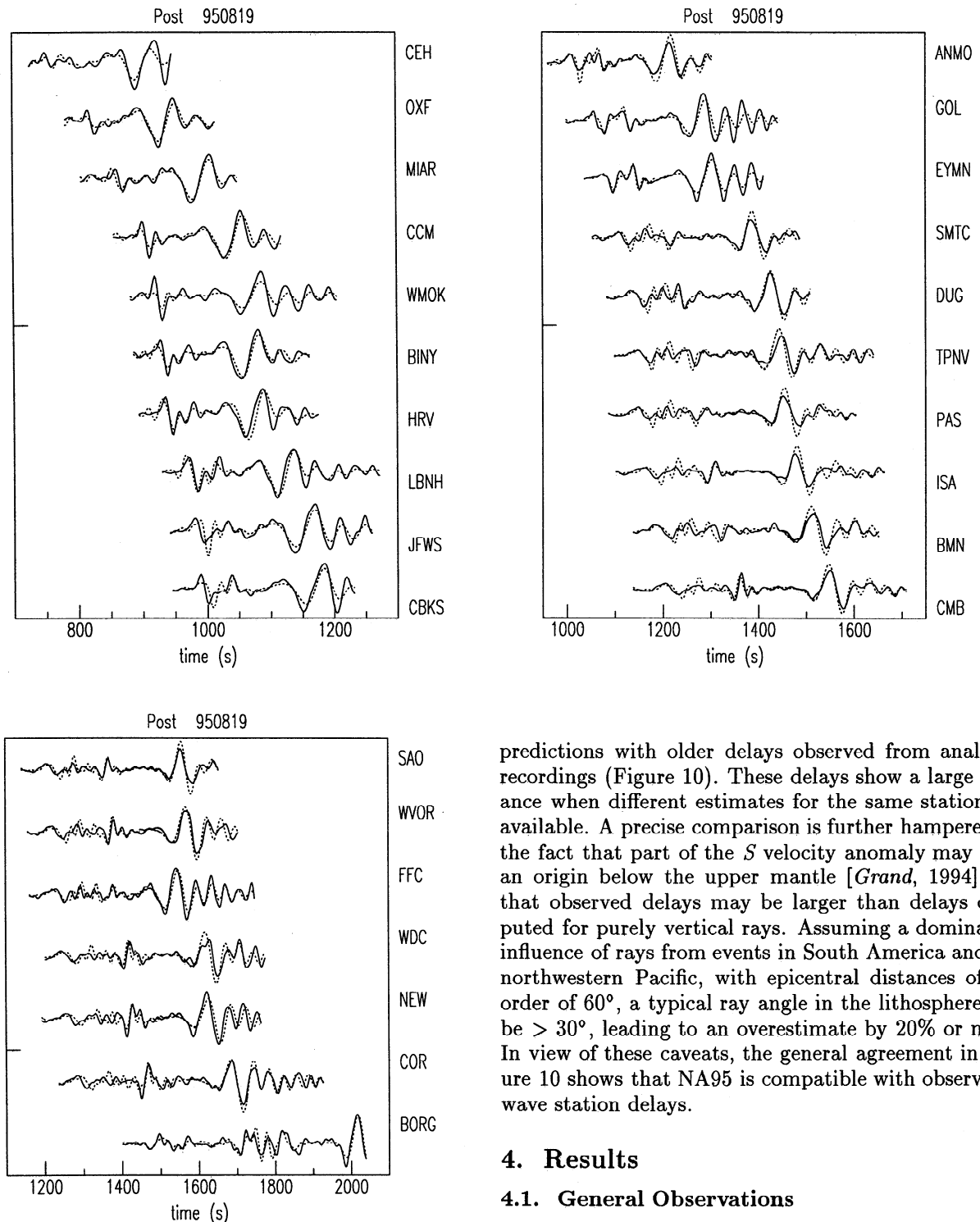
Plate 2. Upper mantle S velocity model NA95 in map view at depths 100–600 km. At 100 km depth the velocity scale saturates at -300 m/s.

Figure 8. A posteriori waveform fits with model NA95, for the data shown in Figure 3.

3.4. Prediction of Vertical Travel Time Delays

Predicted S wave travel time delays can be compared to observations as an independent test for the accuracy of NA95. The predicted delays are computed for a S waves that travel vertically through the upper mantle. Unfortunately, no recent study of S wave station delays in North America is available, so that we compare our

predictions with older delays observed from analogue recordings (Figure 10). These delays show a large variance when different estimates for the same station are available. A precise comparison is further hampered by the fact that part of the S velocity anomaly may have an origin below the upper mantle [*Grand*, 1994] and that observed delays may be larger than delays computed for purely vertical rays. Assuming a dominating influence of rays from events in South America and the northwestern Pacific, with epicentral distances of the order of 60°, a typical ray angle in the lithosphere will be > 30°, leading to an overestimate by 20% or more. In view of these caveats, the general agreement in Figure 10 shows that NA95 is compatible with observed S wave station delays.

4. Results

4.1. General Observations

The S velocity perturbations of NA95 are shown in Plate 2 at six depths. Plates 3–5 show the same model along three vertical cross sections. Our image confirms the existence of a large contrast between the high-velocity North American craton and the low-velocity western margin of North America. While the North American craton has been a tectonically stable area since the Proterozoic, the western United States is tectonically active at present. The Basin and Range province, for example, has recently been extended by a few hundreds of kilometers [*Wernicke et al.*, 1988]. A comparison of NA95 with earlier 1-D models for

Post　950630

Post　950630
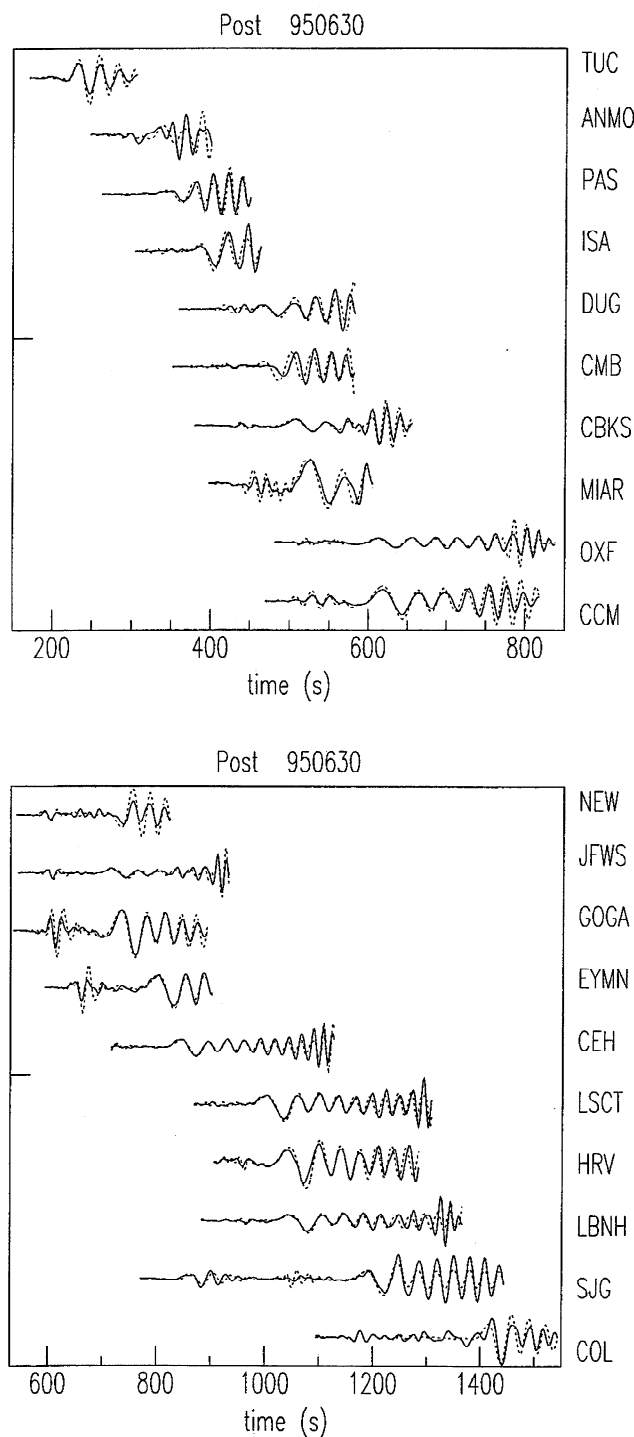
Figure 9. A posteriori waveform fits with model NA95, for the data shown in Figure 4.

these two tectonically contrasting areas of North America yields interesting results. Figures 1a and 1b show velocity-depth profiles at several points through the high-velocity continental root of NA95 and through the low-velocity uppermost mantle beneath the western United States of our model, respectively. Our profiles through the continental root look very similar to the SNA profile from *Grand and Helmberger* [1984] (Fig-

ure 1a), although overall our SV velocities are slightly lower than the SH velocities of SNA. Such small differences have been suggested to be due to anisotropy [e.g., *Gaherty and Jordan*, 1995]. However, our velocity-depth profiles for the western United States (Figure 1b) show much stronger low-velocity anomalies over a narrower depth range than model TNA, derived by *Grand and Helmberger* [1984] for the tectonically active part of North America. Our profiles are in close agreement with a model for the western United States by *Cara* [1979]. Like we do, Cara used SV surface waves while Grand and Helmberger derived TNA from SH body waves. Yet the difference can not be explained simply by anisotropy because in some places the difference is larger than what can reasonably be expected from anisotropy [*Silver*, 1996], and the difference changes sign beneath 200 km. The latter observation makes it likely that the averaging over many paths has flattened velocity gradients in the composite model TNA.

NA95 shows a remarkable transition in the magnitude of velocity anomalies near 150 km depth. Where anomalies in excess of 5% are common at shallower levels, heterogeneity is confined to ±2% at 200 km and deeper. The resolution tests show that we have to be careful in assigning much weight to this observation, since the data allow the model to be damped more strongly at larger depth, even though we still preserve the correct shape of anomalies.

$\square$ +5.0 s　　　$\triangle$ -5.0 s
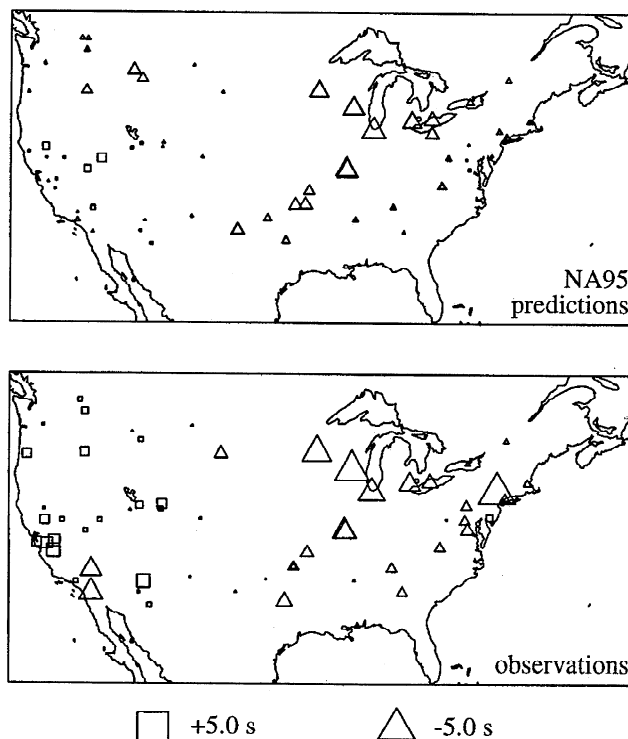
Figure 10. Comparison of delays predicted by NA95, after a baseline correction of −1 s, with observed delays compiled from the literature [*Doyle and Hales*, 1967; *Hales and Roberts*, 1970; *Romanowicz*, 1979; *Romanowicz and Cara*, 1980].
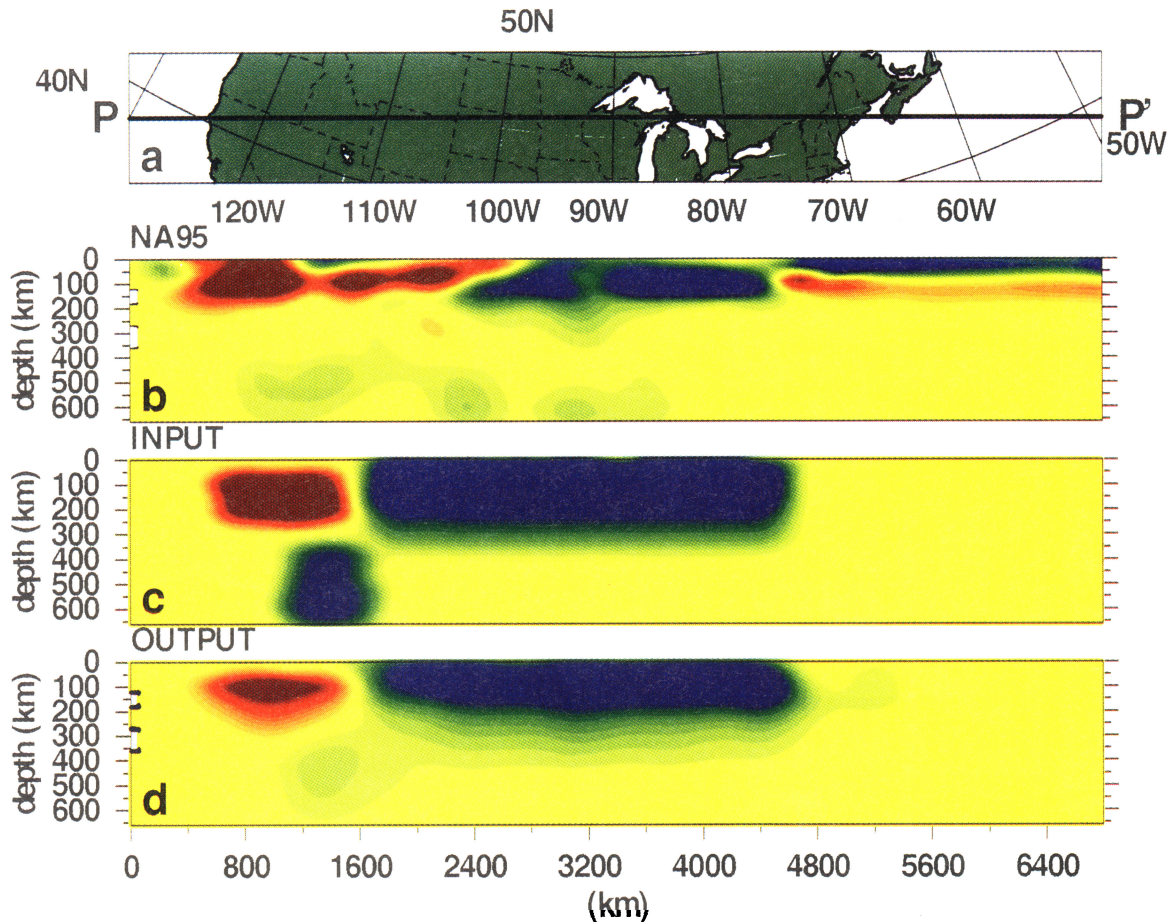
Plate 3. Cross section PP' through NA95. (a) The location of the vertical cross section; (b) the cross section through model NA95; (c) to aid in assessing the resolution, we also plot the results of the resolution test by plotting the synthetic model as well as (d) the retrieved image. See Plate 1 for a map view of the synthetic model.

4.2. Western United States

NA95 reveals a sharper boundary between eastern North America and western North America than previously imaged on this scale. In the uppermost mantle (Plate 2), we observe S velocity perturbations more extreme than -10% west of the Rocky Mountains, beneath California and under the Basin and Range. Such large perturbations have also been found by *Priestley and Brune* [1978] and *Cara* [1979]. Though the extent of the low-velocity region beneath the western United States agrees very well with the more recent results from *Grand* [1994] and *Alsina et al.* [1996], anomalies in NA95 are roughly twice as large.

We do not believe that the NA95 values of the order of -10% are significantly affected by a trade-off with crustal thickness. First of all, directly below the Moho, where a 10 km change in crustal thickness can trade off with a 4% velocity anomaly, the velocities are less extreme than in the asthenosphere, as can be seen from Figure 1b. Second, the crustal thicknesses in NA95 in the region agree well with those of *Braile et al.* [1989]. Neither do we think the amplitudes are the consequence of insufficient damping. If we artificially limit anomalies to lie between -5% and +5%, the variance reduction

drops unacceptably from 84% to 57%. Plate 1 shows that a low-velocity anomaly at 100 km depth is reconstructed with almost correct amplitude.

Consequently, we think that the velocities beneath the western United States are indeed very low ($\ll$ -5%). Such low S velocities cannot be the effect of a thermal anomaly alone but imply the presence of volatiles (water) and/or partial melt in the uppermost mantle. Such a state of the mantle could be the result of upwelling low-viscosity mantle material that filled the space of a slab window created by cessation of subduction of the Farallon plate [*Atwater*, 1970; *Dickinson and Snyder*, 1979; *Dickinson*, 1997]. Alternatively, volatiles could have been released into the slab window from the subducted Farallon plate, which continued to sink through the upper mantle. The low velocities related to the slab window extend at least as far down as 300 km (Plate 2) and are at that depth surrounded to the north and south by high-velocity anomalies. These anomalies and the high-velocity anomalies in the transition zone beneath the western United States and Mexico are interpreted in detail by *Van der Lee and Nolet* [1997] as the image of the subducted trailing fragments of the Farallon plate. *Bird* [1988] proposed that the subducting Farallon plate has removed much of the lithosphere
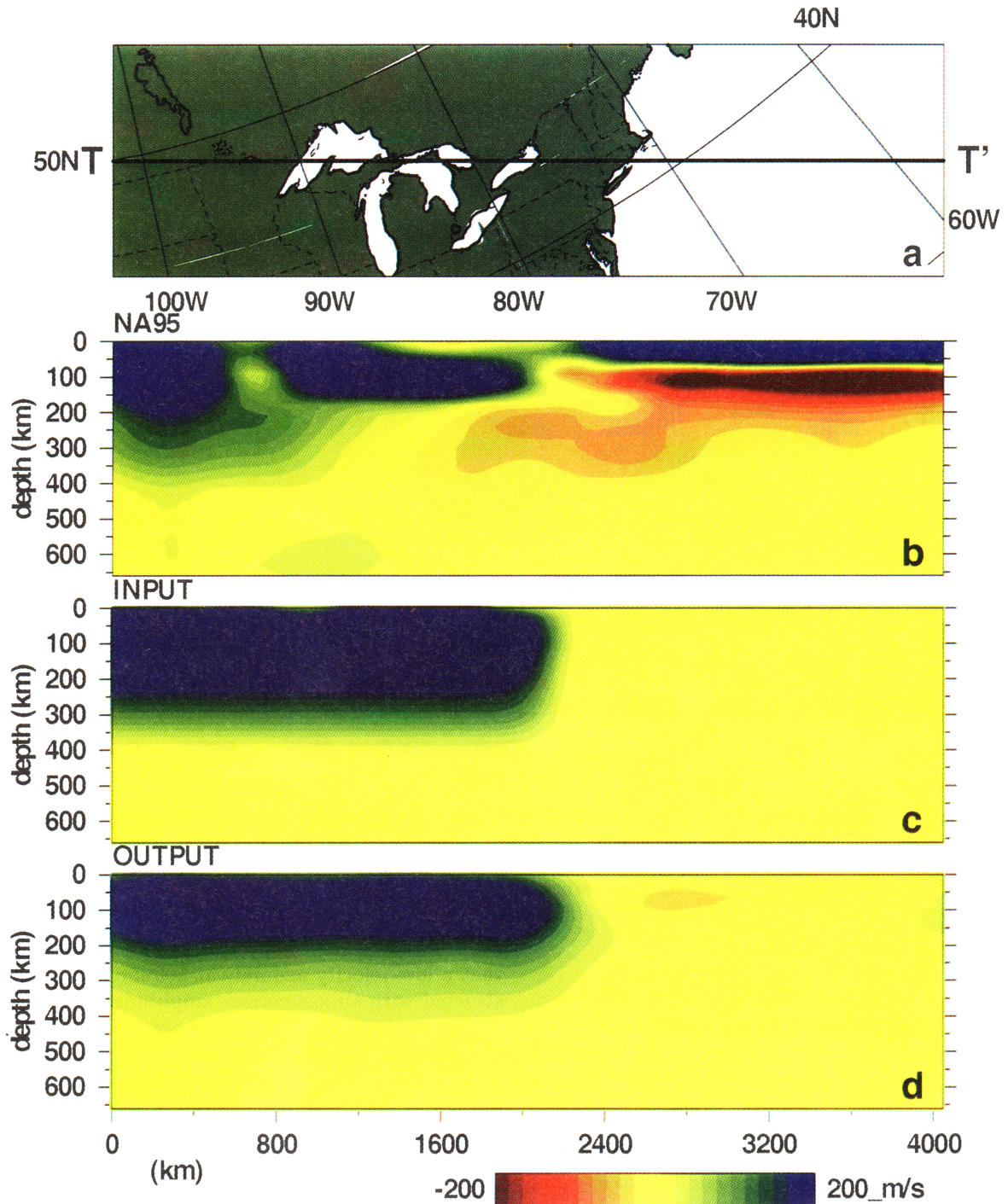
Plate 4.   Same as Plate 3, except for cross section TT'.

4.3. Yellowstone and the Colorado Plateau

of the western United States. His model is supported by the absence of a seismically visible lithosphere in our model beneath the western United States. The extremely low velocities imaged in NA95 seem to be located directly beneath the crust, although this should be reevaluated after future addition of constraints from higher-frequency seismograms and shorter wave paths.

We have also imaged low velocities 200 to 300 km deep in the upper mantle beneath the Cascade volcanoes in Oregon and Washington (Plate 2). These are likely related to ongoing arc volcanism in this region due to subduction of the Juan de Fuca plate.

We have imaged a streak of low velocities parallel to the Yellowstone hotspot track, confirming similar findings by *Alsina et al.* [1996]. These low velocities are possibly related to the migration of the Yellowstone mantle plume, and their presence at 300 km would imply a deep origin for the plume, although *Dueker and Sheehan* [1997] offer an alternative explanation of the low-velocities beneath the Yellowstone hotspot track in terms of regional extension across the track.

The Colorado plateau, like the Basin and Range, is also directly underlain by very low S velocities (Plate
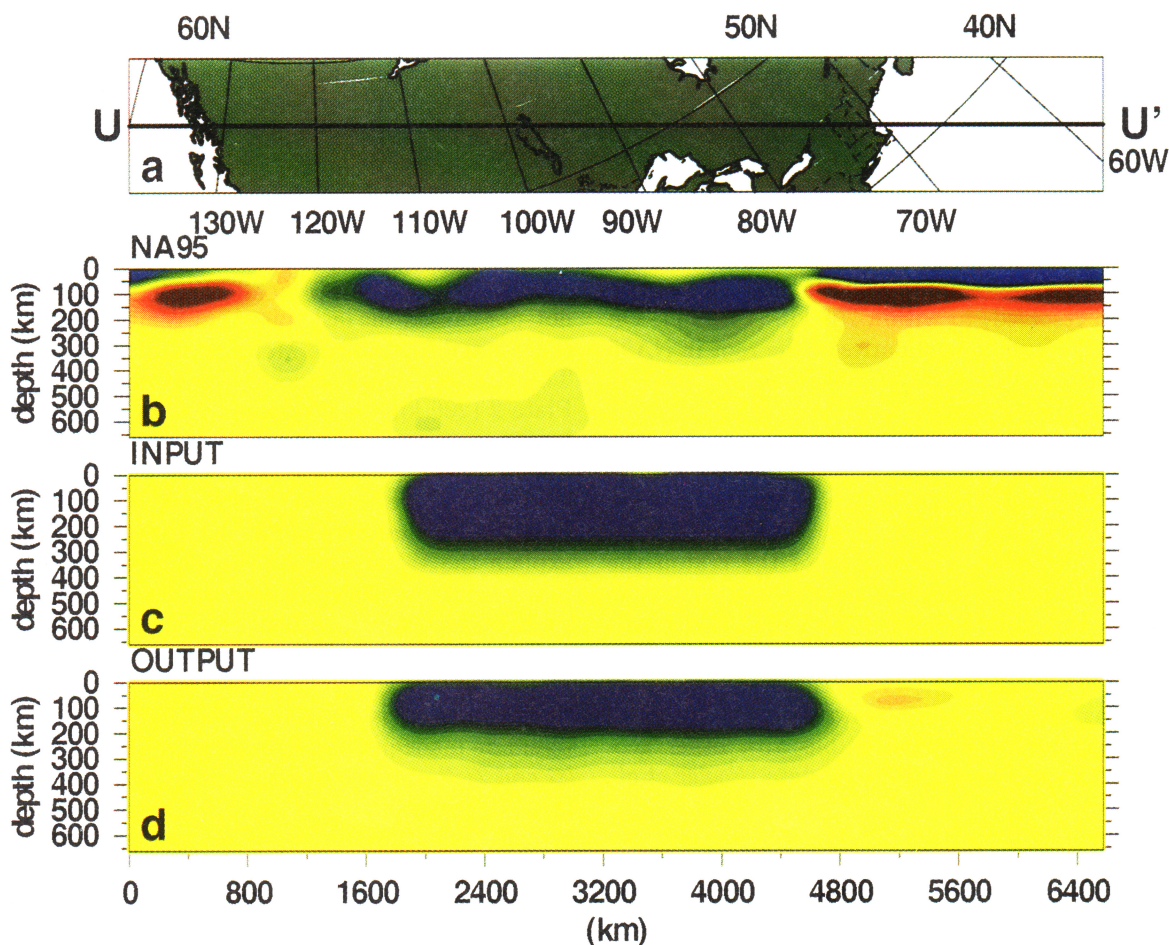
Plate 5. Same as Plate 3, except for cross section UU'.

2). The area of the Colorado Plateau differs from the rest of the western united States because it has been a part of the core of the North American plate since the Proterozoic [*Hoffman*, 1988]. Both Basin and Range extension and the uplift of the Colorado Plateau have been suggested to be different responses to the kinematics and dynamics of the plate interactions between the North American and the subducting Farallon plate [*Cross*, 1986].

4.4. Mexico

In northern Mexico we find an elongated arm of low velocities beneath and parallel to the Sierra Madre Occidental. Although Plate 1 indicates that a velocity structure beneath the western United States may be smeared southeastward, the smearing is not nearly enough to explain this arm of very low velocities. *Alsina et al.* [1996] image a similar low-velocity arm in northern Mexico, although it is wider and offset to the east in their image. The Sierra Madre Occidental was a volcanic arc related to subduction of the Farallon plate during the Paleogene but is now underlain by the southern part of the slab window [*Dickinson and Snyder*, 1979], and the northern Sierra Madre Occidental is presently undergoing similar extension as the Basin and Range province in the United States [*Henry and Aranda-Gómez*, 1992]. The low-velocity arm beneath the Sierra Madre occidental extends south to the triple junction, near 20°N,

104°W, of the Colima Graben with the Tepic-Zocoalco graben and the Trans Mexican Volcanic Belt. These grabens separate the Jalisco block from the rest of Mexico through present-day rifting [*Stock and Lee*, 1994; *DeMets et al.*, 1995]. The low velocities in this area must be related to this rifting process, and NA95 shows that the low velocities extend down to depths of at least 200 km. Moving parallel to the Middle America trench, the pattern of low velocities resumes east of the 93°W, at 100 to 200 km beneath the Isthmus of Tehuantepec (Plate 2). In between, beneath Guerrero, no low velocities have been imaged, which is most likely due to the absence of a mantle wedge caused by flat subduction of the Cocos plate [*Pardo and Suárez*, 1995]. This area is on the edge of where NA95 is well resolved, and future work with regional data is necessary to confirm this inference.

4.5. The Craton

East of the Rocky Mountains we have imaged a large nonhomogeneous area of high S-velocities. These represent the continental root of of the North American craton of Archean and Proterozoic age [*Jordan*, 1975]. The S velocity anomaly of the craton is of the order of +4%, and this anomaly appears well resolved in Plate 1. Plates 3c–d, 4c–d, and 5c–d show that only the bottom 50 km of a 300 km deep anomaly would be damped in in the tomographic model, but would still be visible.

From Plates 3b, 4b and 5b we therefore conclude that the anomaly is reliably resolved over the full depth of 200-250 km over which we see it.

At shallow levels (100 km, Plate 2) the variation in values of the S velocity in this area is high and possibly due in part to unresolved trade-offs with crustal heterogeneity. This variability decreases with depth (Plate 2). The spatial resolution of the cratonic high-velocity region is very good and smooth boundaries of the region are very well resolved, to within 200 km (Plate 1). On a large scale the lateral boundaries of the root in NA95 agree well with results from *Grand* [1994], but it also has interesting new detail.

The eastern and southern edge of the craton follow closely the trend of the Grenville-Appalachian border [*Hoffman*, 1988] and directly east of it the crust is underlain by a very thin lithosphere and low-velocity asthenosphere. On the western side of the craton the high-velocity root does not extend beneath Wyoming (Plates 2, 3, 4, and 5) which was already suggested by the results of *Grand* [1994]. Although this was initially an unexpected result, given the Archean age of the Wyoming province, the absence of a root beneath Wyoming appears to be compatible with other geophysical, geochemical and geological data [*Eggler et al.*, 1988].

We find from cross section TT' (Plate 4) that the root is the thinnest in the northeastern United States and in southeastern Canada where it does not not extend beneath 200 km. Farther northwest in cross section TT', the root extends as deep as 350 km beneath the Superior province. The Archean Superior province is very large [*Hoffman*, 1988] and is also sampled by cross sections UU' and PP' (around 4000 km and 3200 km distance, respectively). Cross sections UU' and PP' show that most of the continental root, underlying areas of "juvenile" Proterozoic crust [*Hoffman*, 1988], does not extend deeper than 250 km. This agrees with *Ricard et al.* [1996], who show that a continental root as deep as 300 km is not necessary to explain global phase velocity measurements.

Far below the solidus, where effects of anelasticity do not have a significant influence, a temperature decrease of about 130° is needed to effectuate an increase of 1% in the S velocity [*Duffy and Anderson*, 1989; *Nolet and Zielhuis*, 1994]. A negative temperature anomaly that is sufficiently large to explain the 4% velocity high would require permanent subsidence of the craton of the order of 2-3 km. Although recurrent subsidence and uplift of several kilometers characterize the tectonic history of the craton [*Leighton*, 1996], there is no evidence for such permanent subsidence. Except for Hudson Bay, which is still subject to postglacial rebound, we find Precambrian rock uplifted above sea level. Therefore the high S velocities of the continental root cannot just be thermally induced, and a compositional difference must be present [*Jordan*, 1988].

4.6. The Atlantic Margin

A V-shaped dent of low velocity is imaged in the high-velocity region of the continental root beneath New England around 45°N. The location of the dent corresponds well with the area where significant changes in S wave splitting characteristics are found [*Barruol et al.*, 1997; *Fouch and Fischer*, 1996; *Fischer et al.*, 1996] while *Taylor and Toksöz* [1979] and *Levin et al.* [1995] found deep low P velocities here in an early tomographic study. The Great Meteor and Monteregian hotspots passed through this region at around 180 and 100 Ma, respectively [*Morgan*, 1983]. The Monteregian hotspot caused the last episode of White Mountains plutonism and formed the Monteregian Hills [*Sleep*, 1990]. The strength of its imposed signature in the image of Plate 2 (200 km) is surprisingly large. The S velocities here are some 2% lower than those of the surrounding continental root and 4% lower than the highest S velocities of the root. If this is a thermal effect, temperature anomalies of of 250° and 500° are required to explain the velocities. As this is above the estimated temperature anomaly of even an active mantle plume, we need to invoke chemical heterogeneity as an explanation. Since both the lithospheric root and and the plume are thought to have undergone similar depletion processes [*Phipps Morgan et al.*, 1995], this mechanism would be inadequate to explain such heterogeneity. *Nolet and Zielhuis* [1994] have proposed a model for enrichment of the edges of lithospheric roots caused by deep dehydration of subducting slabs. They regard the low P velocities of *Taylor and Toksöz* [1979] as evidence that hydration processes were active during subduction of the Iapetus plate. The increased temperature associated with a rising mantle plume through the deep hydrated region may have melted some of the lithospheric root. Petrological evidence for the presence of water in the mantle comes from lamprophyres from New England [*Eby*, 1985].

The low velocities in the V-shaped dent extend to the deeper upper mantle and connect to a deep low-velocity region beneath and parallel to the Appalachians. This zone of low velocities extends down to the transition zone (Plate 2), which confirms early results for P velocity anomalies from *Romanowicz* [1979]. Since heat conduction computations show that a 1000° thermally anomalous vertical dike representing Mesozoic rifting of the Atlantic would have been reduced to less than a 1% S velocity anomaly at present, we think these low velocities can be explained by the presence of water in the mantle [*Nolet and Zielhuis*, 1994], dating back from subduction of the Iapetus plate.

NA95 shows high lithospheric S velocities at depths less than 100 km beneath the Atlantic Ocean (Plates 3-5). Beneath 100 km the oceans are underlain by a classic low-velocity zone with velocity anomalies around -6%. In the westernmost Atlantic, just east of the continental platform, high lithospheric velocities continue as deep as 180 km, which can also be seen in the results of *Grand* [1994]. In this area the Atlantic oceanic plate reaches its oldest age of 180 m.y.

Appendix: Inversion

Our inversion method differs in several details from that outlined by *Nolet* [1990]. Here we only emphasize

these differences. For a more complete description of the method the reader is referred to *Nolet* [1990].

A.1. Waveform Fits

The misfit of a synthetic seismogram is defined as

$$F(\gamma) = \int w^2(t)[\boldsymbol{R}d(t) - \boldsymbol{R}s(t,\gamma)]^2 dt, \qquad (A1)$$

where $d(t)$ is the recorded seismogram and $s(t,\gamma)$ is the synthetic seismogram, which depends on the model parameters γ. $\boldsymbol{R}$ is a filtering and windowing operator, and $w(t)$ is a weighting function designed, using the inverse of the signal envelope, to enhance the contribution to the misfit of the higher modes with respect to the naturally dominating fundamental mode. In earlier applications of PWI, $\boldsymbol{R}$ represented a simple boxcar window and frequency cutoff to isolate the signals of interest. We improved $\boldsymbol{R}$ to minimize effects of wraparounds and ringing by using a 44% cosine tapered time domain window and identically tapered frequency domain filter. This improvement is important when the fundamental mode time window is separated from the higher modes to allow for different filters and when scattered waves are cut from direct waves, but it does not make a significant difference when an entire wave train with naturally tapered edges is considered [*Van der Lee*, 1996].

The model parameters γ_i represent the S velocity as a function of depth, except for one that represents the crustal thickness [*Das and Nolet*, 1995]. The average S velocity perturbations along the path between source and receiver, $\overline{\delta\beta(r)}$, are given in terms of basis functions $h_i(r)$ of radius, whereas the path-averaged Moho depth δH is a discrete model parameter, which needs a slightly different treatment:

$$\begin{aligned} \overline{\delta\beta(r)}/\sigma_\beta &= \sum_{i=1}^{M-1} \gamma_i h_i(r) \\ \overline{\delta H}/\sigma_H &= \gamma_M \end{aligned} \qquad (A2)$$

where σ_β and σ_H are the estimated standard deviations of the distribution of existing S-velocities and Moho depths, respectively. Diagonalization of the Hessian of $F(\gamma)$ around the minimum at $\gamma = \gamma_{opt}$ provides new parameters η_j that have uncorrelated uncertainties and are linear combinations of the γ_i:

$$\boldsymbol{\eta} = \boldsymbol{S}^T \boldsymbol{\gamma} \qquad (A3)$$

where the rows of $\boldsymbol{S}^T$ are the eigenvectors of the Hessian matrix. The eigenvalues of the Hessian are used to compute the uncorrelated standard deviations $\Delta\eta_i$ [*Nolet*, 1990] The transformation gives

$$\begin{aligned} \overline{\delta\beta(r)}/\sigma_\beta &= \sum_{j=1}^{M} \eta_j g_j(r) \\ \overline{\delta H}/\sigma_H &= \sum_{j=1}^{M} \eta_j g_j^H \end{aligned} \qquad (A4)$$

where

$$\begin{aligned} g_j(r) &= \sum_{i=1}^{M-1} S_{ji}^T h_i(r) \\ g_j^H &= S_{jM}^T \end{aligned} \qquad (A5)$$

For the pth path we write

$$\begin{aligned} \overline{\delta\beta(r)} &= \frac{1}{\Delta_p} \int_{P_p} (\beta(r,\theta,\phi) - \beta_p^0(r)) \, d\Delta \\ \overline{\delta H} &= \frac{1}{\Delta_p} \int_{P_p} (H(\theta,\phi) - H_p^0) \, d\Delta \end{aligned} \qquad (A6)$$

where Δ_p is the epicentral distance along great circle path P_p. The parameters $\beta_p^0(r)$ and H_p^0 are the background S velocity model and Moho depth, respectively, along P_p. We multiply (A4) with dual basis functions $(\tilde{g}_i(r), \tilde{g}_i^H)$ that are orthogonal to $(g_j(r), g_j^H)$ in the sense that

$$\frac{1}{L} \int g_i(r) \tilde{g}_j(r) dr + g_i^H \tilde{g}_j^H = \delta_{ij} \qquad (A7)$$

where $\delta_{ij} = 0$ if $i \neq j$ and $\delta_{ij} = 1$ if $i = j$, to obtain the following constraint equations:

$$\frac{1}{\Delta_p} \frac{1}{L} \int_{P_p} \int_{R_d}^{R_0} \frac{\beta(r,\theta,\phi) - \beta_p^0(r)}{\sigma_\beta} \tilde{g}_i(r) dr d\Delta +$$

$$\frac{1}{\Delta_p} \int_{P_p} \frac{H(\theta,\phi) - H_p^0}{\sigma_H} \tilde{g}_i^H d\Delta = \eta_i \pm \Delta\eta_i, \quad (A8)$$

where R_0 is the Earth's radius and R_d is some radius in the lower mantle below which structural perturbations do not significantly affect the waveforms in the time window and frequency band of interest and L is a characteristic depth range.

Thus, for each path we have M constraint equations which are linear in the model perturbations. Combining all paths together results in a system of linear independent constraints on three-dimensional Earth structure.

A.2. Linear Inversion

The parameters we estimate from the constraints are 3-D perturbations to a 1-D reference model $(\beta_0(r), H_0)$. We have, however, used different background models $(\beta_p^0(r), H_p^0)$ in the waveform fitting for each path. We therefore rewrite the constraint equation (A8) for the ith constraint of the pth great circle path:

$$\frac{1}{\Delta_p} \frac{1}{L} \int_{P_p} \int_{R_d}^{R_0} \frac{\beta(r,\theta,\phi) - \beta_0(r)}{\sigma_\beta} \tilde{g}_i(r) dr d\Delta +$$

$$\frac{1}{\Delta_p} \int_{P_p} \frac{H(\theta,\phi) - H_0}{\sigma_H} \tilde{g}_i^H d\Delta = \zeta_i \pm \Delta\zeta_i \quad (A9)$$

where

$$\zeta_i = \eta_i + \frac{1}{\Delta_p} \frac{1}{L} \int_{P_p} \int_{R_d}^{R_0} \frac{\beta_p^0(r) - \beta_0(r)}{\sigma_\beta} \tilde{g}_i(r) dr d\Delta$$

$$+ \frac{1}{\Delta_p} \int_{P_p} \frac{H_p^0 - H_0}{\sigma_H} \tilde{g}_i^H d\Delta$$

$$\Delta\zeta_i = \Delta\eta_i. \qquad (A10)$$

Likewise, different values for σ_β and σ_H can be used for each path if desired. We now identify $\delta\beta(r,\theta,\phi) = \beta(r,\theta,\phi) - \beta_0(r)$ and $\delta H(\theta,\phi) = H(\theta,\phi) - H_0$ as the 3-D perturbations in Earth structure that we wish to estimate. The datum on the right hand side, ζ_i, is determined from the waveform fits and is corrected for the background model. The kernels $\tilde{g}_i(r)$ and $\tilde{g}_i^H$ are determined by the great circle ray path and the sensitivity of the waveforms to different model depths; $\tilde{g}_i^H$ can be considered as a geometrical element of Hilbert vector $\tilde{g}_i(r)$. We then discretize the problem by expanding $\delta\beta(r,\theta,\phi)$ and $\delta H(\theta,\phi)$ into a finite number of basis functions:

$$\begin{aligned} \delta\beta(r) &= \sum_{k=1}^{K_\beta} \mu_k f_k(r) \\ \delta H(\theta,\phi) &= \sum_{k=K_\beta+1}^{K} \mu_k h_k(\theta,\phi). \end{aligned} \quad (A11)$$

Insertion of (A11) into (A9) transforms the system into a system of linear equations, which we wish to solve for $\boldsymbol{\mu}$, which has $K = K_\beta + K_H$ elements. We introduce the matrix elements

$$\Gamma_{ik} = \begin{cases} \frac{1}{\Delta_p L} \int_{P_p}^{R_0} \int_{R_d} f_k(r)\tilde{g}_i(r)drd\Delta & \text{if } 1 \le k \le K_\beta \\ \frac{1}{\Delta_p} \int_{P_p} h_k(\theta,\phi)\tilde{g}_i^H d\Delta & \text{if } K_\beta < k \le K \end{cases} \quad (A12)$$

The data vector is ζ and has as many elements as the total number of constraints from all seismograms. We have grouped the factors $1/\sigma_{\delta\beta}$ and $1/\sigma_{\delta H}$ into a diagonal matrix denoted by $C_\mu^{-1/2}$, where C_μ is the a priori covariance matrix for the model perturbations. We then scale the equations to unit variance, using $C_d^{-1/2}$, the diagonal matrix of standard deviations $\Delta\zeta_i$. Together this gives the system of linear constraints:

$$C_d^{-1/2} \Gamma C_m^{-1/2} \boldsymbol{\mu} = C_d^{-1/2} \zeta. \quad (A13)$$

We proceed using $\boldsymbol{m} = C_\mu^{-1/2}\boldsymbol{\mu}$ as the unknown model perturbation vector and $G = C_d^{-1/2}\Gamma$ as the matrix of data kernel projections. On the right-hand side, we use $q = C_d^{-1/2}\zeta$ as the data. Model $\boldsymbol{m}$ is dimensionless, and in order to obtain its physical values we simply multiply $\boldsymbol{m}$ with $C_\mu^{1/2}$. Thus we have

$$G\boldsymbol{m} = q. \quad (A14)$$

Zielhuis and Nolet [1994] define $\boldsymbol{m}$ by cells of constant velocity on a geographical grid. This has the disadvantage that cell dimensions can vary considerably with latitude or depth. In order to prevent biases introduced by variable cell size and to optimize the mapping from r to grid indices, we introduce an equidistant (Cartesian) grid of knots. The spherically symmetric reference model remains defined as a function of radius r, and this model includes all important discontinuities. However, the depth to the Moho is varied in our inversion, using

parameters defined on a nearly equidistant triangular grid of knots [*Wang and Dahlen*, 1995]. We define trilinear interpolation between the knots on the Cartesian grid, that is,

$$\frac{\delta\beta(r)}{\sigma_\beta} = \sum_{k=k_1}^{k_8} m_k f_k(|x-x_k|,|y-y_k|,|z-z_k|), \quad (A15)$$

and

$$f_k(x,y,z) = \left(1 - \frac{|x-x_k|}{dx}\right)\left(1 - \frac{|y-y_k|}{dy}\right) \cdot \\ \left(1 - \frac{|z-z_k|}{dz}\right) \quad \text{if} \begin{cases} |x-x_k| \le dx \\ |y-y_k| \le dy \\ |z-z_k| \le dz \end{cases} \quad (A16)$$

where dx, dy, and dz are the grid spacing in the x, y, and z direction, respectively, and k_1 through k_8 are the indices of the eight corners of the cell in which r is located. The functions f_k may be directly inserted in (A12). Similarly, for the triangular grid we have

$$\frac{\delta H(\theta,\phi)}{\sigma_H} = \sum_{k=k_1}^{k_3} m_k h_k(\theta,\phi,\theta_k,\phi_k). \quad (A17)$$

Let Δ_{k_1} be the epicentral distance between (θ,ϕ) and $(\theta_{k_1},\phi_{k_1})$, and let $\Delta_\perp$ be the epicentral distance between $(\theta_{k_1},\phi_{k_1})$ and the closest point on the great circle through the other two corners of the triangle in which (θ,ϕ) is located and of which $(\theta_{k_1},\phi_{k_1})$ is a corner. We define

$$h_k(\theta,\phi,\theta_k,\phi_k) = r_k\left(1 - \frac{\Delta_k}{\Delta_\perp}\right) \quad (A18)$$

where the r_k are such that

$$\sum_{k=k_1}^{k_3} h_k = 1. \quad (A19)$$

The functions h_k may also be directly inserted in (A12). We position the Cartesian grid such that its origin coincides with the center of the Earth and 47°N, 83°W determines the direction of the z axis in the grid. In the center of the model, the z, x, and y directions are good approximations for the depth (radius) and the transverse (longitude, latitude) directions, respectively, but away from the center this is no longer true.

A.3. Smoothing

Underdetermined as they are, tomographic inversions usually result in erratic models if regularized by simple minimization or damping of the model norm. We require a priori that the model μ is smooth. This means that we can express $\boldsymbol{m} = S\boldsymbol{n}$, where S is a smoothing matrix. So we have

$$H\boldsymbol{n} = q \quad (A20)$$

where $H = GS$ and $m = Sn$. The elements of S for the Cartesian grid can be written as

$$S_{ij} = \begin{cases} r_j \left(1 - \frac{\Delta r_{ij}}{dr}\right) \left(1 - \frac{\Delta t_{ij}}{dt}\right) & \text{if} \begin{cases} \Delta r_{ij} < dr \\ \Delta t_{ij} < dt \end{cases} \\ 0 & \text{otherwise} \end{cases}$$
(A21)

where the r_j are such that

$$\sum_{j=1}^{K_\beta} S_{ij} = 1.$$
(A22)

where the r_j are such that

$$\sum_{j=1}^{K_\beta} S_{ij} = 1.$$
(A23)

where Δr_{ij} and Δt_{ij} are the radial and transverse distances between knots i and j, and dr and dt are the smoothing lengths in the radial and transverse direction, respectively. For transverse smoothing dr should not exceed the grid spacing by too much, whereas dt should reach over several grid points. For the triangular grid the elements of S become

$$S_{ij} = \begin{cases} r_j \left(1 - \frac{\Delta t_{ij}}{dt}\right) & \text{if } \Delta t_{ij} < dt \\ 0 & \text{if } \Delta t_{ij} \geq dt \end{cases}$$
(A24)

$$\sum_{j=K_\beta+1}^{K} S_{ij} = 1.$$
(A25)

Alternatively, we may choose to not compute explicitly a smoothing matrix S but adopt transversely smooth basis functions from the start and compute H directly without computing G first. We define

$$\frac{\beta(r)}{\sigma_\beta} = \sum_{l=1}^{L} w_l \sum_{j=1}^{J_l} \frac{1}{J_l} \sum_{k=k_1^{lj}}^{k_8^{lj}} n_k f_k^{lj},$$
(A26)

where

$$f_k^{lj} = f_k(|x_{lj} - x_k|, |y_{lj} - y_k|, |z_{lj} - z_k|)$$
(A27)

and the functions f_k are again trilinear interpolation functions. Imagine a shell of constant radius through point k. The sum over l on this shell is a sum over L concentric circles, with radii Δ_l, around point k. The Δ_l are smaller than the smoothing distance dt. The average contribution from each circle is computed with J_l steps along the circle and is weighted with w_l. The smoothing weights w_l depend linearly on the distance to point k,

$$w_l(\Delta_l) = r_l(1 - \frac{\Delta_k}{dt})$$
(A28)

where the r_l are such that

$$\sum_{l=1}^{L} w_l = 1.$$
(A29)

The coordinates of r are represented by (x_{11}, y_{11}, z_{11}). Expression (A26) is simpler for the triangular grid:

$$\frac{H(\theta, \phi)}{\sigma_H} = \sum_{k=1}^{K_\beta} n_k s_k(\theta, \phi, \theta_k, \phi_k)$$
(A30)

$$s_k(\theta, \phi, \theta_k, \phi_k) = \begin{cases} r_k \left(1 - \frac{\Delta_k}{dt}\right) & \forall \Delta_k < dt \\ 0 & \forall \Delta_k \geq dt. \end{cases}$$
(A31)

where the r_k are such that

$$\sum_{k=K_\beta+1}^{K} s_k = 1.$$
(A32)

The elements of H are

$$H_{ik} = \begin{cases} \frac{1}{\Delta\zeta_i} \frac{1}{\Delta_p} \int_{P_p} \int_{R_d}^{R_o} \sum_{l=1}^{L} w_l \sum_{j=1}^{J_l} f_k^{lj} \tilde{g}_i(r) dr d\Delta \\ \qquad\qquad\qquad\qquad \text{if } 1 \leq k \leq K_\beta \\ \frac{1}{\Delta\zeta_i} \frac{1}{\Delta_p} \int_{P_p} s_k(\theta, \phi) \tilde{g}_i^H d\Delta & \text{if } K_\beta < k \leq K. \end{cases}$$
(A33)

Although the two ways of smoothing are very similar, we prefer the latter as it uses a much finer discretization. Apart from this, the two ways are equivalent and a choice between the two may depend on the availability of processing time and disk space. We use basis functions with radii of $240r/R$ km perpendicular to r, where R is the Earth's radius and r is the radius to the grid point. This limits the resolving power to maximal spherical harmonic degree $l \approx 83$, assuming that structures with length scales smaller than 240 km can not be resolved.

A.4. Regularized Inversion

We use the least squares algorithm "LSQR" from *Paige and Saunders* [1982a] to solve (A20). We add regularization equations to (A20) that bias the non-smoothed solution n toward zero norm. The system then becomes

$$\begin{pmatrix} H \\ \lambda I \end{pmatrix} n = \begin{pmatrix} q \\ o \end{pmatrix}.$$
(A34)

The parameter λ determines the strength of the damping. The objective function is now

$$\|Hn - q\|^2 + \lambda^2 \|n\|^2,$$
(A35)

so that both misfit and Euclidean norm of n are simultaneously minimized by LSQR. Since $m = Sn$ is the smooth version of n, we are damping the curvature of model m when we damp the norm of n. To speed up convergence, we scale the columns of H with the weights

$$w_j = \frac{1 + \nu}{|c_j| + \nu|c_m|}$$
(A36)

where $|c_j|$ is the Euclidean norm of the jth column of H of which $|c_m|$ is the maximum, and $\nu = 0.1$ [*Paige*

and Saunders, 1982b; *VanDecar and Snieder*, 1994]. Although the solution is uniquely determined by minimizing (A35), scaling helps to reduce a possible bias from wave path geometry that may be present if the inversion is not run to full convergence.

After scaling H with the w_j, which implies scaling n with W^{-1}, we still want to damp the norm of n and not that of $W^{-1}n$. System (A34) thus becomes

$$
\begin{aligned}
\begin{pmatrix} A \\ \lambda W \end{pmatrix} x &= \begin{pmatrix} q \\ o \end{pmatrix} \\
A &= HW \\
x &= W^{-1}n \\
W_{ij} &= \delta_{ij} w_j,
\end{aligned} \tag{A37}
$$

which is equivalent to (A34) except for the intrinsic scaling.

References

Ahern, T., and Members of the FDSN, *Federation of Digital Seismograph Networks Station Book,* Inc. Res. Inst. for Seismol., Seattle, Wash., 1994.

Alsina, D., R.L. Woodward, and R.K. Snieder, Shear wave velocity structure in North America from large-scale waveform inversions of surface waves, *J. Geophys. Res., 101,* 15969–15986, 1996.

Anderson, D.L., and H. Spetzler, Partial meling and the low velocity zone, *Phys. Earth Planet. Inter., 4,* 62–64, 1970.

Atwater, T., Implications of plate tectonics for the Cenozoic tectonic evolution of western North America, *Geol. Soc. Am. Bull., 81,* 3513–3536, 1970.

Barruol, G., P.G. Silver, and A. Vauchez, Seismic anisotropy in the eastern United States: Deep structure of a complex continental plate, *J. Geophys. Res., 102,* 8329–8348, 1997.

Benz, H.M., G. Zandt, and D.H. Oppenheimer, Lithospheric structure of northern California from teleseismic images of the upper mantle, *J. Geophys. Res., 97,* 4791–4807, 1992.

Bird, P., Formation of the Rocky Mountains, western United States: A continuum computer model, *Science, 239,* 1501–1507, 1988.

Bostock, M.G., and J.C. VanDecar, Upper mantle structure of the northern Cascadia subduction zone, *Can. J. Earth. Sci., 32,* 1-12, 1995.

Braile, L.W., W.J. Hinze, R.R.B. von Frese, and Gr.R. Keller, Seismic properties of the crust and uppermost mantle of the conterminous United States and adjacent Canada, in: *Geophysical Framework of the Continental United States,* edited by L.C. Pakiser and W.D. Mooney, *Mem. Geol. Soc. Am., 172,* 655-680, 1989.

Cara, M., Lateral variations of S velocity in the upper mantle from higher Rayleigh modes, *Geophys. J. R. Astron. Soc., 57,* 649–670, 1979.

Cross, T.A., Tectonic controls of foreland basin subsidence and Laramide style deformation, western United States, *Spec. Publ. Int. Assoc. Sedimentol., 8,* 15–39, 1986.

Das, T., and G. Nolet, Crustal thickness estimation using

high frequency Rayleigh waves, *Geophys. Res. Lett., 22,* 539–542, 1995.

DeMets, C., I. Carmichael, T. Melbourne, O. Sanchez, J. Stock, G. Suárez, and K. Hudnut, Anticipating the successor to Mexico's largest historical earthquake, *Eos Trans. AGU, 76,* 417, 424, 1995.

Dickinson, W.R., Tectonic implications of Cenozoic volcanism in coastal California, *Geol. Soc. Am. Bull.,* in press, 1997.

Dickinson, W.R., and W.S. Snyder, Geometry of subducted slabs related to San Andreas transform, *J. Geol., 87,* 609–627, 1979.

Doyle, H.A., and A.L. Hales, An analysis os the travel times of S waves to North American stations in the distance range 20° to 82°, *Bull. Seismol. Am. Soc., 57,* 761–771, 1967.

Dueker, K.G., and A.F. Sheehan, Mantle discontinuity structure from mid point stacks of converted P to S waves across the Yellowstone hotspot track, *J. Geophys. Res., 102,* 8313–8327, 1997.

Duffy, T.S., and D.L. Anderson, Seismic velocities in mantle minerals and the mineralogy of the upper mantle, *J. Geophys. Res., 94,* 1895–1912, 1989.

Dziewonski, A.M., A.L. Hales, and E.R. Lapwood, Parametrically simple Earth models consistent with geophysical data, *Phys. Earth Planet. Inter., 10,* 12–48, 1975.

Dziewonski, A.M., A. Friedman, D. Giardini, and J.H. Woodhouse, Global seismicity of 1982: Centroid-moment tensor solutions for 308 earthquakes, *Phys. Earth Planet. Inter., 33,* 76–90, 1983.

Eby, G.N., Age relations, chemistry, and petrogenesis of mafic alkaline dikes from the Monteregian Hills and younger White Mountain igneous provinces, *Can. J. Earth Sci., 22,* 1103–1111, 1985.

Eggler, D.H., J.K. Meen, F. Welt, F.O. Dudas, K.P. Furlong, M.E. McCallum, and R.W. Carlson, Tectomagmatism of the Wyoming province, *Col. Sch. Mines Q., 83,* 25–40, 1988.

Fischer, K.M., M.E. Wysession, T.J. Clarke, M.J. Fouch, G.I. Al-Eqabi, P.J. Shore, R.W. Valenzuela, A. Li, and J.M. Zaslow, The 1995–1996 Missouri to Massachusetts broadband seismometer deployment, *IRIS News., 15(2),* 6–9, 1996.

Fouch, M.J., and K.M. Fischer, Shear wave splitting beneath the eastern United States, paper presented at 8th Annual IRIS Workshop, Blaine, Wash., 1996.

Gaherty, J.B., and T.H. Jordan, Lehmann discontinuity as the base of an anisotropic layer beneath continents, *Science, 268,* 1468–1471, 1995.

Grand, S.P., Mantle shear structure beneath the Americas and surrounding oceans, *J. Geophys. Res., 99,* 11,591–11,621, 1994.

Grand, S.P., and D.V. Helmberger, Upper mantle shear structure of North America, *Geophys. J. R. Astron. Soc., 76,* 399–438, 1984.

Hales, A.L., Upper mantle models and the thickness of the continental lithosphere, *Geophys. J. Int., 105,* 355–363, 1991.

Hales, A.L., and J.L. Roberts, The travel times of S and SKS, *Bull. Seismol. Am. Soc., 60,* 461–489, 1970.

Helmberger, D.V., G. Engen, and S. Grand, Upper-mantle cross-section from California to Greenland, *J. Geophys., 58,* 92–100, 1985.

Henry, C.D., and J.J. Aranda-Gómez, The real southern Basin and Range: Mid- to late Cenozoic extension in Mexico, *Geology, 20,* 701–704, 1992.

Hoffman, P. F., United plates of America, the birth of a craton: Early Proterozoic assembly and growth of Laurentia, *Annu. Rev. Earth Planet. Sci., 16,* 535–603, 1988.

Humphreys, E.D., and K.G. Dueker, Western U.S. upper mantle structure, *J. Geophys. Res., 99,* 9615–9634, 1994a.

Humphreys, E.D., and K.G. Dueker, Physical state of the western U.S. upper mantle, *J. Geophys. Res., 99,* 9635–9650, 1994b.

Jobert, N. and G. Jobert, Ray tracing for surface waves, in *Seismic Tomography,* edited by G. Nolet, pp. 275–300, D. Reidel, Norwell, Mass., 1987.

Jordan, T.H., The continental tectosphere, *Rev. Geophys., 13,* 1–12, 1975.

Jordan, T.H., Structure and formation of the continental tectosphere, *J. Petrol., Special Lithosphere Issue,* 11–37, 1988.

Kennett, B.L.N., Approximations for surface wave propagation in laterally varying media, *Geophys. J. Int., 122,* 470–478, 1995.

Kennett, B.L.N., and G. Nolet, The interaction of the *S* wavefield with upper mantle heterogeneity, *Geophys. J. Int., 101,* 751–762, 1990.

Knopoff, L., Observation and inversion of surface wave dispersion, *Tectonophysics, 13,* 497–519, 1972.

Leighton, M.W., Interior cratonic basins: A record of regional tectonic influences, in *Basement and Basins of Eastern North America,* edited by B.A. van der Pluijm and P.A. Catacosinos, *Spec. Pap. Geol. Soc. Am. 308,* 77–93, 1996.

Lerner-Lam, A.L., and T.H. Jordan, How thick are the continents?, *J. Geophys. Res., 92,* 14,007–14,026, 1987.

Levin, V., A.L. Lerner-Lam, and W. Menke, Anomalous mantle structure at the Proterozoic-Paleozoic boundary in the northeast US, *Geophys. Res. Lett., 22,* 121–124, 1995.

Levshin, A.L., Effects of lateral inhomogeneities on surface wave amplitude measurements, *Ann. Geophys., 3,* 511–518, 1985.

Marquering, H., and R. Snieder, Surface wave mode coupling for efficient forward modeling and inversion of body wave phases, *Geophys. J. Int., 120,* 186–208, 1994.

Meier, T., S. Lebedev, G. Nolet, and F.A. Dahlen, Diffraction tomography using multimode surface waves, *J. Geophys. Res., 102,* 8255–8267, 1997.

Michaelson, C.A., and C.S. Weaver, Upper mantle structure from teleseismic P wave arrivals in Washington and northern Oregon, *J. Geophys. Res., 91,* 2077–2094, 1986.

Morgan, W.J., Hotspot tracks and the early rifting of the Atlantic, *Tectonophysics, 94,* 123–139, 1983.

Nolet, G., Partitioned waveform inversion and two-dimensional structure under the network of autonomously recording seismographs, *J. Geophys. Res., 95,* 8499–8512, 1990.

Nolet, G., and A. Zielhuis, Low S velocities under the Tornquist-Teisseyre zone: Evidence for water injection into the transition zone by subduction, *J. Geophys. Res., 99,* 15,813–15,820, 1994.

Paige, C.C., and M.A. Saunders, LSQR: An algorithm for sparse linear equations and sparse least squares, *ACM TOMS, 8,* 43–71, 1982a.

Paige, C.C., and M.A. Saunders, ALGORITHM 583 LSQR: sparse linear equations and least squares problems, *ACM TOMS, 8,* 195–209, 1982b.

Pardo, M., and G. Suárez, Shape of the subducted Rivera and Cocos plates in southern Mexico: Seismic and tectonic implications, *J. Geophys. Res., 100,* 12,357–12,373, 1995.

Percival, D.B., and A.T. Walden, *Spectral Analysis for Physical Applications, Multitaper and Conventional Univariate Techniques,* Cambridge Univ. Press, New York, 1993.

Phipps Morgan, J., W.J. Morgan, and E. Price, Hotspot melting generates both hotspot volcanism and a hotspot swell?, *J. Geophys. Res., 100,* 8045–8062, 1995.

Priestley, K., and J. Brune, Surface waves and the structure of the Great Basin of Nevada and western Utah, *J. Geophys. Res., 83,* 2265–2272, 1978.

Rasmussen, J., and E. Humphreys, Tomographic image of the Juan de Fuca plate beneath Washington and western Oregon using teleseismic P-wave travel times, *Geophys. Res. Lett., 15,* 1417–1420, 1988.

Ricard, Y., H. Nataf, and J. Montagner, The 3-SMAC model: Confrontation with seismic data, *J. Geophys. Res., 101,* 8457–8472, 1996.

Romanowicz, B., Seismic structure of the upper mantle beneath the United States by three-dimensional inversion of body wave arrival times, *Geophys. J. R. Astron. Soc., 57,* 479–506, 1979.

Romanowicz, B., On the measurement of anelastic attenuation using amplitudes of low frequency surface waves, *Phys. Earth Planet. Inter., 84,* 179–191, 1994.

Romanowicz, B., A global tomographic model of shear attenuation in the upper mantle, *J. Geophys. Res., 100,* 12,375–12,394, 1995.

Romanowicz, B.A., and M. Cara, Reconsideration of the relations between S and P station anomalies in North America, *Geophys. Res. Lett., 7,* 417–420, 1980.

Saltzer, R., and E. Humphreys, Upper mantle P wave structure of the eastern Snake River Plain and its relationship to geodynamic models of the region, J. Geophys. Res., in press, 1997.

Shankland, T.J., R.J. O'Connell, and H.S. Waff, Geophysical constraints on partial melt in the upper mantle, *Rev. Geophys., 19,* 394–406, 1981.

Silver, P.G., Seismic anisotropy beneath the continents: Probing the depths of geology, *Annu. Rev. Earth Planet. Sci., 24,* 385–432, 1996.

Sleep, N.H., Monteregian hotspot track: A long-lived mantle plume, *J. Geophys. Res., 95,* 21,983–21,990, 1990.

Stock, J.M., and J. Lee, Do microplates in subduction zones leave a geological record?, *Tectonics, 13,* 1472–1487, 1994.

Taylor, S.R., and M.N. Toksöz, Three-dimensional crust and upper mantle structure of the northeastern United States, *J. Geophys. Res., 84,* 7627–7644, 1979.

Tromp, J., and F.A. Dahlen, Variational principles for surface wave propagation on a laterally heterogeneous Earth, II, Frequency-domain JWKB theory, *Geophys. J. Int., 109,* 599–619, 1992.

VanDecar, J.C., and R. Snieder, Obtaining smooth solutions to large, linear, inverse problems, *Geophysics, 59,* 818–829, 1994.

VanDecar, J.C., D.E. James, and M. Assumpção, Seismic evidence for a fossil mantle plume beneath South America and implications for plate driving forces, *Nature, 378,* 25–31, 1995.

Van der Hilst, R.D., Tomography with P, PP and pP delay-time data and the three-dimensional mantle structure below the Caribbean region, dissertation, 250 pp., Utrecht Univ., Geol. Ultraiectina, Utrecht, 1990.

Van der Lee, S., The Earth's upper mantle: Its structure beneath North America and the 660-km discontinuity beneath northern Europe, Ph.D. thesis, 186 pp., Princeton Univ., Princeton, N.J., 1996.

Van der Lee, S., and G. Nolet, The subducted Farallon plate, *Nature, 386,* 266–269, 1997.

Walck, M.C., The P-wave upper mantle structure beneath an active spreading centre: the Gulf of California, *Geophys. J. R. Astron. Soc., 76,* 697–723, 1984.

Wang, Z., and F.A. Dahlen, Spherical-spline parameteriza-

tion of three-dimensional Earth models, *Geophys. Res. Lett., 22*, 3099-3102, 1995.

Wernicke, B., G.J. Axen, and J.K. Snow, Basin and Range extensional tectonics at the latitude of Las Vegas, Nevada, *Geol. Soc. Am. Bull., 100*, 1738–1757, 1988.

Woodward, R.L., and G. Masters, Calibration and data quality of the long-period SRO/ASRO networks, 1977 to 1980, *Bull. Seismol. Soc. Am., 79*, 1972–1983, 1989.

Zielhuis, A., and G. Nolet, Shear-wave velocity variations in the upper mantle beneath central Europe, *Geophys. J. Int., 117*, 695–715, 1994.

G. Nolet, Department of Geosciences, Princeton University, Princeton, NJ 08544. (tel: (609) 258 4128; fax: (609) 258 1274; e-mail: guust@geo.princeton.edu)

S. van der Lee, Department of Terrestrial Magnetism, Carnegie Institution of Washington, 5241 Broad Branch Rd., N.W., Washington, DC 20015. (tel: (202) 686 4370; e-mail: suzan@dtm.ciw.edu)